TECHNICAL MEMORANDUM

764

Convectively coupled Kelvin Waves: From linear theory to global models

M. Herman[1], Z. Fuchs[2,1], D. Raymond[1], P. Bechtold[3]

Research Department

[1]New Mexico Tech, Socorro, New Mexico,[2] Split University, [3]ECMWF

To appear in the J. Atmos. Sci.
The definitive version will be published by the Americ. Meteorol. Soc.

October 13, 2015

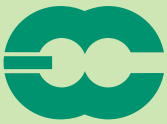

European Centre for Medium-Range Weather Forecasts
Europäisches Zentrum für mittelfristige Wettervorhersage
Centre européen pour les prévisions météorologiques à moyen terme

Series: ECMWF Technical Memoranda

A full list of ECMWF Publications can be found on our web site under:
http://www.ecmwf.int/en/research/publications

Contact: library@ecmwf.int

European Centre for Medium-Range Weather Forecasts
Shinfield Park, Reading, RG2 9AX, England

Abstract

We analyze composite structures of tropical convectively-coupled Kelvin waves in terms of the theory of Raymond and Fuchs using radiosonde data, 3D analysis and reanalysis model output, and annual integrations with the ECMWF model on the full planet and on an aqua-planet. Precipitation anomalies are estimated using the NOAA interpolated OLR and TRMM 3B42 datasets, as well as using model OLR and rainfall diagnostics. Derived variables from these datasets are used to examine assumptions of the theory. Large-scale characteristics of wave phenomena are robust in all datasets and models where Kelvin wave variance is large. Indices from the theory representing column moisture and convective inhibition are also robust. Our results suggest that the CCKW is highly dependent on convective inhibition, while column moisture does not play an important role.

1 Introduction

Raymond *et al.* (2015) distinguish two broad categories of tropical disturbances:

1. In fast-moving disturbances such as equatorial Kelvin waves, mixed Rossby-gravity waves, and inertia-gravity waves, gravity wave dynamics are clearly important.

2. In slow-moving disturbances such as equatorial Rossby waves, easterly waves, monsoon lows, tropical cyclones, and the Madden-Julian oscillation, strong potential vorticity signatures are evident, which indicates a significant role for balanced dynamics.

This dichotomy is evocative of the papers of Yasunaga and Mapes (2012a,b), wherein tropical disturbances are likewise considered members of two distinct groups chiefly characterized by dynamical behavior: rotational and divergent. Although there is much evidence for such a dichotomy, there is also evidence that these categories are less distinct. Roundy (2012b) showed that the OLR power spectrum is continuous between the traditional MJO and convectively-coupled Kelvin wave regimes when the Indian Ocean is analyzed independently. In addition, Roundy (2008) showed that some Kelvin waves are associated with significant rotational anomalies. Since we are chiefly concerned with the causal mechanisms of tropical disturbances in this work, we adopt the notion of distinct categories, while allowing for the possibility that these may interact and may also share characteristics to some degree. For purposes of clarity, we hereafter use the term convectively-coupled Kelvin waves to represent the faster-propagating phenomena ($c \approx 15$ m s^{-1}).

The focus of this paper will be on the fast, gravity-wave category, specifically on convectively coupled Kelvin waves (CCKW). According to the tropical wave mode analysis of Wheeler and Kiladis (1999), these account for the second greatest OLR variance after the Madden-Julian oscillation (MJO) and therefore control a substantial fraction of tropical rainfall variability. We will analyze composite structures of tropical CCKW phenomena in terms of physical parameters that Raymond and Fuchs (2007, hereafter RF07) identified as most significant for CCKWs. In this study, we make use of 3D analysis and reanalysis model output, radiosonde data, as well as output from long integrations with the European Center for Medium-Range Weather Forecasts (ECMWF) model. It is our goal to illustrate the agreement or disagreement between the linear theory of RF07 and observations and then to test the capability of models as well as of reanalyses to manifest observed CCKW characteristics. A broader picture encompasses a similar analysis of all species of tropical disturbance with the Raymond *et al.* (2015) categorization in mind—a goal we are currently pursuing.

Since Matsuno (1966) we have known that Kelvin waves follow a linear theory in the adiabatic atmosphere, but there is still debate on how these waves couple with convection. There are many lin-

ear models that look at CCKWs (e. g., Mapes 2000; Majda and Shefter 2001a,b; Majda *et al.* 2004; Khouider and Majda 2006a,b, 2008; Fuchs and Raymond 2007; Raymond and Fuchs 2007; Kuang 2008a,b; Andersen and Kuang 2008; Fuchs *et al.* 2012) To parameterize precipitation, Mapes used a convective inhibition (CIN) closure that included a separate accounting of the triggering energy, RF07 and Fuchs *et al.* (2012) used deep CIN and moisture closures, while the rest of the mentioned models used a variety of schemes including modified convective available potential energy (CAPE) closures in which CAPE is computed only in the lower troposphere. The RF07 model is unique because it can obtain the observed phase speed, growth rate, and vertical structure of CCKWs without prescribing the phase dependence of the vertical heating profile. In this paper we examine several key diagnostic parameters from the RF07 model to assist in understanding the physics behind the CCKW on data sets obtained from 3D analysis and reanalysis model output, radiosonde data, and special runs of the ECMWF model.

Many cloud-resolving model (CRM) studies consider the CCKW; some are: Grabowski and Moncrieff (2001), Peters and Bretherton (2006), Tulich *et al.* (2007), Tulich and Mapes (2010), Kuang *et al.* (2005), and Fuchs *et al.* (2014). Fuchs *et al.* (2014) used the CRM of Raymond and Zeng (2005) to identify mechanisms primarily responsible for controlling precipitation in CCKWs and linked them to the linear theory of RF07. They showed that saturation fraction (precipitable water divided by saturated precipitable water) and instability index (an indicator of tropospheric stability) anomalies both lag rainfall and are therefore not the primary causal mechanisms for CCKWs, while the deep convective inhibition (DCIN) decrease and its excursion to negative values led the rainfall, suggesting that the CCKW is controlled by DCIN. The latter finding is in agreement with the linear model of RF07.

Radiosonde observations, though limited, can also provide insight into mechanisms controlling the CCKW. An example of a particularly clean CCKW (Straub and Kiladis 2002) was observed during the TEPPS project (Tropical East Pacific Process Study; Yuter and Houze 2000). During this project, the research vessel *Ronald H. Brown* was stationed near 125° W, 8° N for approximately two weeks in August 1997 and launched six radiosondes per day. RF07 analyzed the radiosonde observations from this project to obtain a time series of convective inhibition and saturation fraction. They showed that the deep convection and resulting precipitation were related to the moistening of the atmosphere, but that the onset of precipitation was delayed approximately one day from this moistening by the existence of a stable layer. In this case, CIN played a significant role in the timing of the precipitation. A thorough review on CCKWs can be found in Kiladis *et al.* (2009).

In this paper we will focus on two physical parameters we have found to be important through the linear theory of RF07 and via the CRM experiment of Fuchs *et al.* (2014): DCIN, which depends on free tropospheric temperature variations and boundary layer moist entropy; and saturation fraction. The justification for these parameters is as follows:

1. Deep convection has been shown to occur sporadically in the tropics, while shallow or congestus clouds occur almost continuously in some areas. Raymond (1995) proposed a mechanism whereby deep convective events are controlled by a boundary-layer quasi-equilibrium existing between the boundary layer and the lowest levels of the free troposphere. Over timescales of $1/2$ d, a state of statistical equilibrium occurs whereby boundary layer moist entropy anomalies are soon followed by the vertical mass flux of entropy into and out of the layer, which maintains the equilibrium state. This generally prevents the instability needed to drive a deep convective event such that extra forcing is required. Mapes (2000) posits that one culprit is the gust fronts driven by the deep convection itself. While there is a chicken-and-egg causality issue inherent in this theory, it is nevertheless an idea with considerable empirical support. A truly external agent, however, is the temperature anomaly driven by the forced ascent and descent of a passing atmospheric wave. When the lower free troposphere is adiabatically warmed via wave activity alone, convective inhibition

is increased, suppressing the nearly continuous convection. During the next phase of the wave, this inhibiting layer vanishes, allowing parcels with anomalously greater moist entropy to convect beyond the original inhibition layer. Based on in situ observations in the tropical east Pacific from data collected during the East Pacific Investigation of Climate (EPIC2001), Raymond *et al.* (2003), found that the existence of even a weak stable layer just above the planetary boundary layer (PBL) is sufficient to inhibit the development of deep convection and associated precipitation. This confirms earlier results of Firestone and Albrecht (1986) obtained from dropsonde measurements in the tropical Pacific. Lastly, the mathematical theory of RF07 as well as the CRM results of Fuchs *et al.* (2014) suggest that DCIN is the primary mechanism responsible for the onset of the CCKW, though the effects of surface moist entropy fluxes have also been shown to be important in CCKWs (Raymond *et al.* 2003; Back and Bretherton 2005; Maloney and Esbensen 2005).

2. Bretherton *et al.* (2004) analyzed passive microwave satellite observations and found that precipitation is highly correlated with the saturation fraction of the troposphere. Sobel *et al.* (2004) reached similar conclusions using data taken near Kwajalein Atoll. Results from numerical cloud models also support this conclusion (Lucas *et al.* 2000; Derbyshire *et al.* 2004; Raymond and Zeng 2005). The linear model of RF07 shows that a correlation of precipitable water with precipitation is of primary importance for the moisture mode—an instability mechanism linked to the observed correlation between column moisture and rainfall considered by some to be related to the MJO. In contrast, the Kelvin mode is only weakly associated with column moisture changes. Yasunaga and Mapes (2012a) found that precipitable water variations were small and did not exhibit a consistent phase relationship with precipitation in CCKWs compared to that of equatorial Rossby waves and the MJO. In the part of the wavenumber-frequency spectrum containing the greatest CCKW precipitation variance, they found no significant lag between precipitable water and rainfall. Roundy and Frank (2004) also found that precipitable water is only weakly modulated in the CCKW spectrum when compared to spectra for equatorial Rossby waves and the MJO.

In our study, we employ the wave-filtering and linear regression techniques used by Straub and Kiladis (2002), Kiladis *et al.* (2009), Straub *et al.* (2010), and others. These techniques comprise a useful toolkit with which one can test the assumptions of theoretical wave models. This paper is organized as follows: physical parameters of interest are defined and their usage in the RF07 linear model are presented in section 2; the data, wave filtering, and linear regression techniques used are described in section 3; comparison between the results of linear theory, observations, reanalysis and ECMWF model integrations is given in section 4; while conclusions are drawn in section 5.

2 Linear theory of RF07

We will here briefly review the linear theory of RF07 and also define the convective inhibition and precipitable water indices used in RF07 and in the CRM experiment of Fuchs *et al.* (2014).

Convective inhibition is an expression of the energy a parcel needs in order to rise to the level of free convection in a conditionally unstable atmosphere. It is thus an expression of the inhibiting layer that isolates a parcel from where it should become positively buoyant. This quantity is typically expressed as the difference between the virtual temperature of a parcel and that of the environment integrated over the logarithm of pressure below the level of free convection. Fuchs *et al.* (2014) used a simplified linear

index, deep convective inhibition (DCIN):

$$\text{DCIN} = s_t^* - s_{bl} \quad , \tag{1}$$

where s_t^* is the saturated moist entropy averaged over a threshold layer in the free troposphere above the nominal boundary layer and s_{bl} is the moist entropy averaged over the nominal boundary layer. The average moist entropy in the boundary layer mostly depends on radiation, surface fluxes and downdrafts while the threshold moist entropy–a proxy for the lower free-tropospheric temperature–depends on radiation, adiabatic lifting, and diabatic heating during moist convective events. Free-tropospheric temperature anomalies driven by convection necessarily have short timescales unless there is forcing from large-scale waves. DCIN will be small or negative if there are anomalously high values of s_{bl}, as in the case of a moist anomaly in the boundary layer, or in the presence of slightly cooler than average temperatures within the threshold layer, leading to lower values of s_t^*.

The RF07 linear model parameterized the contribution to precipitation by convective inhibition as

$$P_2 = P_{2s} - P_{2t} \quad ,$$

where

$$P_{2s} = \mu_{CIN} \lambda_s E \quad , \tag{2}$$

and

$$P_{2t} = \mu_{CIN} \lambda_t b(D) \quad . \tag{3}$$

P_{2t} is related to variations in the buoyancy, b, of the lower free troposphere and is very similar to perturbations in the threshold saturated moist entropy term s_t^* in (1). The coefficient μ_{CIN} is a parameter that governs the sensitivity of the precipitation rate to deep convective inhibition, λ_t represents the sensitivity of precipitation to buoyancy anomalies at a height $z = D$, and $b(D)$ is the scaled buoyancy anomaly at D (taken to be 2.5 km). P_{2s} represents the contribution to precipitation from surface flux variations and is closely related to perturbations in the boundary layer moist entropy s_{bl} in (1), λ_s is a constant representing the sensitivity of convective inhibition to the surface evaporation rate and E is the scaled surface evaporation rate anomaly. The two contributions to precipitation, P_{2t} and P_{2s}, represent the effects of convective inhibition due to lower-tropospheric temperature variations as well to surface fluxes.

The saturation fraction is defined as the precipitable water divided by the saturated precipitable water, and is approximated here by

$$S \approx \frac{\int_0^h \rho (s - s_d) dz}{\int_0^h \rho (s^* - s_d) dz} \quad , \tag{4}$$

where the integrals are taken from the surface to the tropopause height, h, s is the moist entropy and s_d is the dry entropy. The contribution to precipitation from the precipitable water (as defined in the context of the model) in the RF07 model is:

$$P_1 = \alpha \int_0^h q(z) dz \quad , \tag{5}$$

where q is the scaled mixing ratio and α is a moisture adjustment rate taken to be $1/\text{d}$. For clarity, we will hereafter refer to this index as the column moisture.

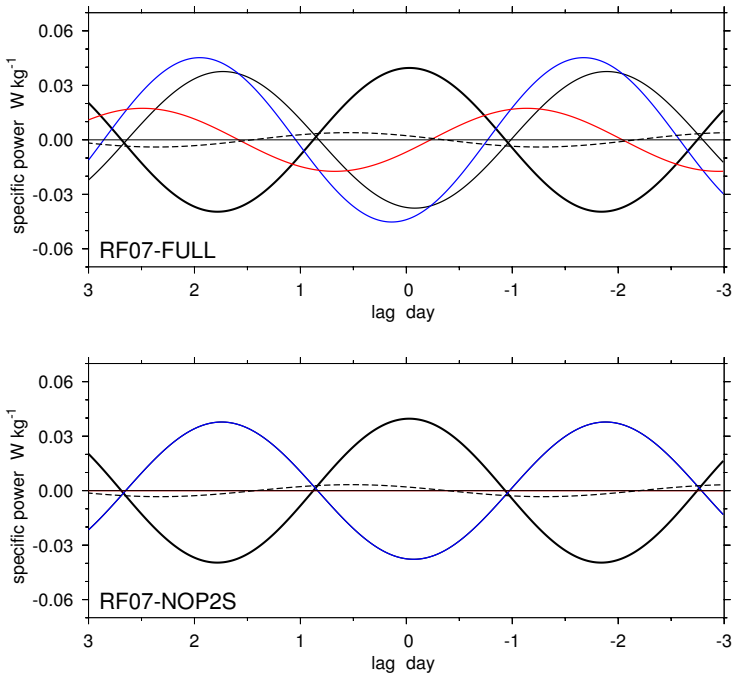

Figure 1: Decomposition of precipitation as a function of lag time for the eastward-moving convectively coupled gravity mode with zonal wavenumber $l = 7$ from the RF07 linear model (RF07; left) and for the case when surface fluxes are set to zero (RF07-NOP2S; right). The total precipitation (thick solid black line), DCIN (thin solid black line), the threshold buoyancy anomaly P_{2t} (blue line), the boundary layer moist entropy anomaly P_{2s} (red line), and the column moisture (dashed line) are shown. The zero axis is plotted for reference. All variables have units of specific power ($W\,kg^{-1}$). In the RF07-NOP2S case, DCIN is aligned with P_{2t}.

The total precipitation in the RF07 model was the sum of the terms defined above where P_1 represents the moisture closure and P_2 the DCIN closure:

$$P \sim P_1 + P_{2s} - P_{2t} \quad . \tag{6}$$

Figure 1 shows the various contributions to the total precipitation as a function of lag time with respect to the precipitation maximum for the eastward-moving convectively coupled gravity mode that maps onto the Kelvin mode in a rotating atmosphere with zonal wavenumber $l = 7$. This is the wavenumber of maximum growth rate for the Kelvin mode of the RF07 model. Time evolves from right to left in these and in other similar plots in this study. For comparison to other published CCKW composite structures plotted on a longitude axis, the East is to the right of the rain maximum in our study. The plot on the top shows the complete model (hereafter RF07-FULL), while the plot on the bottom shows an altered model where no surface flux anomalies enter the precipitation calculation (hereafter RF07-NOP2S). Note that we have inverted the plot of P_{2t} from RF07 to facilitate interpretation of figures; thus, $P_{2t} > 0$ represents a positive threshold buoyancy anomaly. Corresponding plots in RF07 actually show $-P_{2t}$.

The total precipitation, (6), is given by a thick solid black line, the column moisture contribution P_1 by a dashed line, the total DCIN contribution by a thin solid black line, the DCIN contribution due to buoyancy variations above the PBL P_{2t} given in blue, and the surface flux contribution P_{2s} in red. In RF07-FULL, most of the precipitation is associated with P_{2t}, i. e., the reduction of DCIN as a result of wave-induced cooling above the PBL. There is a significant contribution to the precipitation from P_{2s},

but this has a smaller effect. This is consistent with the result of RF07 that turning off wind-induced surface heat flux exchange (WISHE) causes only minor changes in CCKW mode behavior.

This effect is illustrated in RF07-NOP2S, where $\lambda_s = 0$, so that no surface flux anomalies can enter the precipitation anomaly. As in RF07-FULL, the DCIN minimum slightly leads the precipitation anomaly. Only the column moisture contribution causes the rainfall to slightly lag the DCIN. The key difference here is that DCIN is driven entirely by the lower-tropospheric saturated moist entropy anomaly P_{2t}. Since P_{2s} is originally small, however, this has little effect on the precipitation between RF07-FULL and RF07-NOP2S. This change also has minimal effect on the propagation speed, growth rate, or vertical temperature structure (not shown). This insensitivity to surface flux anomalies was also found by Kuang (2008a) in CRM simulations of convectively-coupled waves.

RF07 found that the Kelvin mode instability in both RF07-NOP2S and RF07-FULL occurs when DCIN is included in the convective heating closure of the vertically-resolved model. Since this mode is unstable when DCIN is the *only* significant contributor to the heating, it follows that DCIN is a mechanism that can destabilize this wave mode by itself. In contrast, Fuchs and Raymond (2007) found that changes in column-integrated tropospheric moisture acting alone could not destabilize this mode. Since this instability occurs even when DCIN is a function only of the lower-tropospheric temperature anomaly, as in RF07-NOP2S, it follows that the latter is the primary forcing agent of this mode. Lastly, since the model's closure mechanism assumes that DCIN modulates rainfall, the resulting Kelvin mode instability is consistent with the idea that DCIN drives the rainfall of CCKWs.

Very little contribution to the precipitation comes from the column moisture perturbation P_1. This model result is in agreement with the near-invisibility of the equatorial Kelvin wave in the satellite–observed precipitable water field (Roundy and Frank 2004; Yasunaga and Mapes 2012a,b). To summarize, the DCIN contribution to precipitation is by far the most significant, while the precipitable water contribution is negligible. Interestingly the moisture mode in RF07 has very different characteristics (not shown) and opposite to the CCKW: the precipitable water anomaly contribution to precipitation is the most significant for wavenumbers in the CCKW spectrum, while the CIN contribution plays smaller role.

Thermodynamic values entering the indices used in this study are scaled as in RF07 such that all indices and the rainfall have units of specific power: W kg^{-1}. The precipitation is therefore scaled using:

$$P = \frac{gL}{C_p T_R \rho_s} \hat{P},$$

where $g = 9.81$ m s^{-2} is the acceleration of gravity, $L = 2.5 \times 10^6$ J kg^{-1} is the latent heat of vaporization, $C_p = 1005$ J K^{-1} kg^{-1} is the specific heat of dry air at constant pressure, $T_R = 300$ K is a reference temperature, $\rho_s = 1.18$ kg m^{-3} is an assumed surface air density, and $\hat{P}$ is the observed (or modeled) surface precipitation flux anomaly in kg m^{-2} s^{-1} (alternately, the surface rainfall in mm s^{-1}). Where OLR is used as a proxy for the rainfall, it is scaled using $\hat{P} = -4.72 \times 10^{-6} \times \widehat{OLR}$ based on a comparison between Kelvin wave anomalies during the TEPPS project. The boundary layer moist entropy and free-tropospheric saturated moist entropy indices—and therefore the DCIN as well—are scaled using:

$$P_{2s} = \frac{g}{C_p} \mu_{CIN} \hat{s}_{bl}$$

and

$$P_{2t} = \frac{g}{C_p} \mu_{CIN} \hat{s}_t^*$$

where $\mu_{CIN} = 0.38$ m s^{-1}, estimated from a CCKW observation in RF07, $\hat{s}_{bl}$ is the observed boundary layer moist entropy anomaly, and $\hat{s}_t^*$ is the threshold saturated moist entropy anomaly. Both entropy anomalies are in J K^{-1} kg^{-1}. The column moisture anomaly is scaled using:

$$P_1 = \alpha \frac{gL}{C_p T_R} \int_0^h \hat{r}_v dz,$$

where $1/\alpha = 86400$ s, $h = 15000$ m is the assumed depth of the troposphere, and $\hat{r}_v$ is the water vapor mixing ratio in g g^{-1}.

Hereafter, we define the pressure limits of the $\hat{s}_t^*$ layer as $p = [550, 800]$ hPa and those of the $\hat{s}_{bl}$ layer as $p = [850, 1000]$ hPa. We choose these limits based on the idea that lower-tropospheric quasi-equilibrium, rather than boundary layer quasi-equilibrium, controls deep tropical convection. This is supported by the CRM experiments of Kuang (2008a) as well as the empirical and modeling study of Raymond *et al.* (2015). While the threshold layer is deeper than that used in RF07, we have verified that the linear model gives similar results for a deeper threshold layer (not shown). Also, the definition of the nominal boundary layer doesn't enter the linear model, as the boundary layer moist entropy anomaly is assumed there to be strictly proportional to surface moisture flux anomalies.

3 Data and methodology

We now describe the data and analysis techniques used in our study. The datasets used are summarized in Table 1.

3.1 Data

The radiosonde data used in this study were obtained from the Integrated Global Radiosonde Archive (IGRA). Temperature, pressure, relative humidity, wind speed and direction are available in this dataset at a time resolution of $\Delta t \geq 1/2$ d. Majuro Atoll $(171.38°, 7.08°)$ is the West Pacific station closest to the peak variance in the global CCKW signal, as determined from variance maps derived from filtered rainfall estimates (see Figure 2). Koror $(134.48°, 7.33°)$, Yap $(138.08°, 9.48°)$, Chuuk $(151.85°, 7.47°)$, Ponape $(158.22°, 6.97°)$, and Kwajalein Atoll $(167.73°, 8.73°)$ are island stations near Majuro along the northern edge of the CCKW variance maximum; we hereafter refer to these stations collectively as the WPAC group. We also examine data from a larger group of 41 stations including the WPAC group located elsewhere around the tropical band. The positions of all stations used in this study are shown in Figure 2. Filled circles indicate the locations of the WPAC group and white circles indicate the remaining stations.

Reanalysis model output is obtained from the ERA-Interim dataset produced by ECMWF, hereafter ERAI. These data are available on $0.7° \times 0.7°$ grids at 6 h time resolution, though we only use the 00Z and 12Z observations to match those of the radiosonde data. Also, we interpolate the horizontal axes to $1° \times 1°$ resolution for simplicity. Forecast model analysis is obtained from the FiNaL global tropospheric analysis dataset generated in concert with NCEP's Global Forecast System (GFS). These data are available on $1° \times 1°$ grids at 6 h temporal resolution, though we again use only the 00Z and 12Z analyses. This dataset is only available at lower spatial resolutions previous to July 1999. In order to use complete yearly cycles, we thus use FNL analysis data only after January 2000. Unlike the ERAI dataset, which uses a single version of the ECMWF model, the FNL analysis is generated from a model

*Table 1: Parameters for datasets used in this study. A dash indicates field is not applicable for this dataset. Each dataset is categorized as either a proxy for precipitation (*rain*) or as a thermodynamic dataset (*thermo*). Where two resolutions are shown, a slash (/) indicates both are used; an arrow (→) indicates that the resolution was changed for all regressions. All resolutions refer to the dataset, not to the originating model or sensing instrument. The last column,* proxy*, indicates the rain proxy predictor variable(s) used in the linear regressions for each thermodynamic dataset:* N *(NOAA OLR),* T *(TRMM 3B42),* EO *(ECMWF OLR), and* ER *(ECMWF rainfall rate). The asterisk (*) indicates this variable is only used in the Appendix.*

Dataset	type	Δt (d)	Δx (deg)	time span	proxy
NOAA OLR	rain	0.5	2.5→1.0	1982-2013	N
TRMM 3B42	rain	0.125/0.5	0.25/1.0	1998-2013	T
ECMWF OLR	rain	1.0	1.0	various	EO
ECMWF rainfall rate*	rain	1.0	1.0	various	ER
IGRA	thermo	0.5	—	1982-2013	N, T
ERAI	thermo	0.25→0.5	0.7→1.0	1998-2013	N, T
FNL	thermo	0.25→0.5	1.0	2000-2013	N, T
T255-OPANA	thermo	1.0	1.0	2008-2013	N, T, EO, ER*
T255_LAND	thermo	1.0	1.0	8 years	EO
T159-AQUA-NODEEP	thermo	1.0	1.0	4 years	EO
T159-AQUA-DEEP	thermo	1.0	1.0	4 years	EO
T799-AQUA-NODEEP	thermo	1.0	1.0	4 years	EO
T799-AQUA-DEEP	thermo	1.0	1.0	4 years	EO
T1279-AQUA-NODEEP	thermo	1.0	1.0	4 years	EO

whose algorithms have changed over the time interval used. All variables mentioned for the IGRA data are also available for ERAI and FNL.

Proxies of surface precipitation rate are obtained from the Tropical Rainfall Measuring Mission (TRMM), a joint project of the National Aeronautics and Space Administration (NASA) and the National Space Development Agency of Japan (NASDA). We chose the 3B42 dataset based on spatial coverage and for its thoughtful precipitation estimation algorithm. The 3B42 dataset is comprised of an ensemble of satellite passive microwave and infrared (IR) measurements calibrated to precipitation radar, which are then adjusted to agree with temporal means of ground-based rain-gauges. Wherever and whenever the calibrated microwave data are available they are used, otherwise, the calibrated IR is used. The available spatial resolution is $\Delta x = 0.25^\circ$, with 3 h time resolution—though we again limit this to 12 h to facilitate comparison with the other datasets. When using 3B42 with 3D data and model output, we interpolate the horizontal axes to $1^\circ \times 1^\circ$ to match. Although error estimates are included in this dataset, we give all data equal weight in our study in the interest of simplicity and to maximize coverage and availability. In addition we use the NOAA Interpolated OLR dataset, also with twice-daily temporal resolution but only $2.5^\circ \times 2.5^\circ$ horizontal resolution. The original satellite observations have been interpolated in time, which leads to a minimal smoothing effect. For convenience, we interpolate the NOAA OLR to $1^\circ \times 1^\circ$ to match other datasets.

We also employ output from long integrations with the ECMWF forecast model as well as from several special runs of this model—each with spatial resolution of $1^\circ \times 1^\circ$ and temporal resolution of 1 d. The rainfall proxy in this case is an OLR diagnostic generated by the model's own radiation scheme. We investigate the difference between the model OLR and the model rainfall in the Appendix. We also examine the operational analyses between 2008-2012 that include improved physics and data assimila-

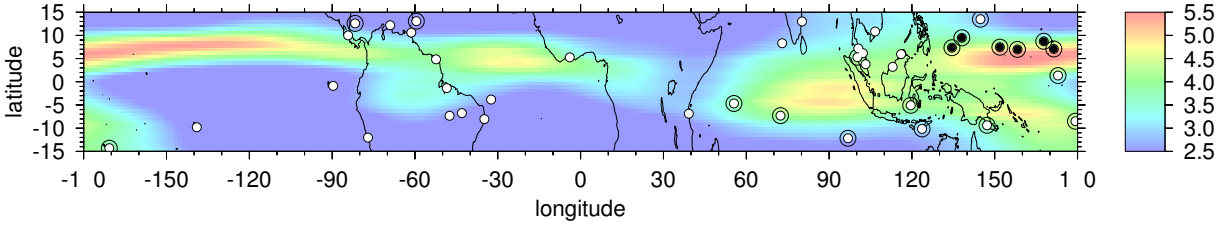

Figure 2: Map of IGRA radiosonde stations used in this study atop contours of KELVIN filter variance for TRMM derived precipitation rates over 1998-2013. Station locations are indicated by circles. The WPAC group circles are filled. Stations that survive the discrimination procedure also have concentric circles. Continents have been outlined for reference. Units are mm d^{-1}.

tion (Bechtold *et al.* 2008) compared to what is employed in the ERAI (which is representative for the 2006 operational model cycle). The operational analysis data has been truncated to the same resolution as ERAI which is T255 ($\Delta x \approx 80$ km); hence, we refer to the operational analysis as T255-OPANA. A model version with the same resolution (T255-LAND) is also run for eight 1-year simulations, each initialized from observations, but run freely thereafter to illustrate how the ECMWF model performs when no data is assimilated.

We also employ a set of aqua-planet versions of the ECMWF model. We use low resolution ($\Delta x \approx 125$ km; hereafter T159-AQUA), medium resolution ($\Delta x \approx 25$ km; hereafter T799-AQUA), and high resolution ($\Delta x \approx 16$ km; hereafter T1279-AQUA) versions. For the lower resolution integrations, we also check the difference between simulations with (DEEP) and without (NODEEP) the deep convective parameterization scheme. The highest resolution integration is only run without the deep convective scheme. The latter has the resolution of the current operational forecast model. In the absence of orography, these models exhibit robust wave signatures that are obvious using minimal time series. We thus perform only four 1-year simulations for each aqua-planet model. The deep convective parameterization in the ECMWF model is a mass-flux scheme based on the relaxation of CAPE anomalies and includes entrainment (Bechtold *et al.* 2008). The model also contains a stratiform precipitation scheme that is never turned off in our simulations.

3.2 Wave filtering

Discrete Fourier transforms (DFT) are performed on each rainfall proxy along the time and longitude dimensions separately at each latitude. Consecutive years are ingested as one time series into the temporal DFT, otherwise years are processed one at a time. The wavenumber-frequency domain is then reduced to a subset including only the spectrum of interest. We reduce the spectrum using two different filters: a large Kelvin-filter window (hereafter KELVIN), similar to that used in Wheeler and Kiladis (1999); and also a narrow-band filter in frequency and wavenumber (hereafter MONO) in order to compare with the monochromatic theory of RF07. For KELVIN, a rectangular filter is used to define boundaries in equivalent depth, $h_e = [8, 90]$ m, and oscillation period, $T = [2.5, 17]$ d, such that all coefficients outside these bounds are set to zero. For MONO, we employ a tapered window to mitigate the appearance of unwanted side lobes in the resulting space-time domain. This filtering window retains the Fourier coefficients of a central dimensionless zonal wavenumber, $k_{z0} = 7$, as well as fractions of the coefficients on either side within the interval $k = [3, 11]$. The frequency spectrum is given a similar treatment with central frequency $f_0 = 0.22$ cycles per day ($T = 4.5$ d), and interval $f = [0.12, 0.32]$ cycles per day. These central values were chosen to match the most unstable Kelvin mode in the RF07 model. Linear functions defined on these intervals weight coefficients ranging from zero at the bounds to one at the central value. All other

coefficients in the domain are set to zero. The original space-time domain is then reconstructed using inverse Fourier transforms, resulting in a wave-filtered dataset. Since each filtered rainfall proxy only retains the portion of the spectrum including the wave species of interest, it comprises an approximate basis upon which to construct wave composites. A notable caveat is that the filtered proxy also contains other phenomena that project onto the selected wavenumbers and frequencies.

3.3 Linear regression

We next make the simplifying assumption that all thermodynamic anomalies coinciding with Kelvin-wave events correlate at some lag to the associated precipitation event, here represented by the wave-filtered rainfall proxies. To this end, we perform linear regressions of all variables in the atmospheric column above each location of interest using each available wave-filtered rainfall proxy as a predictor variable in the regression. We thus solve the following equation using a least-squares regression at each location, at each vertical level, and at each discrete lag time up to three days from the actual time:

$$\hat{\chi}_i(t+\delta t_j) = A_{ij} + B_{ij}\hat{P}(t) \quad , \tag{7}$$

where $\hat{\chi}_i$ is the ith thermodynamic variable (including the rainfall) observed at some location and vertical height of interest, t is the time axis over which data and model output are observed or diagnosed, $\delta t_j = j\Delta t$ is the resolution-dependent temporal lag, $\hat{P}(t)$ is the observed or diagnosed wave-filtered rainfall proxy timeseries at the location of interest, A_{ij} is the χ_i-intercept at some lag j, and B_{ij} is the predicted slope of $\hat{\chi}_i$ versus $\hat{P}$ at lag j. The result is a set of coefficients that allow us to reconstruct the χ_i-P relationship along the lag axis using an assumed value for the rainfall anomaly at $j = 0$:

$$\chi_i(\delta t_j) = A_{ij} + B_{ij}P_0 \quad , \tag{8}$$

where $P_0 = 50$ mm d^{-1} is the assumed rainfall anomaly in all cases. This value matches the time-averaged rainfall measured during the TEPPS Kelvin-wave passage (Straub and Kiladis 2002); the wave passage also coincided with an OLR anomaly of 125 W m^{-2}.

We found good correspondence in the variables of interest among stations in the WPAC group for IGRA, ERAI, FNL, T255-OPANA. We found broader correspondence for these locations in T255-LAND. We then averaged each 8 together for each variable from the WPAC group to form composites representing the West Pacific for each rainfall proxy and for each wave filter. These composites are given names such as IGRA-NOAA-KELVIN, representing the WPAC group from the IGRA radiosonde dataset, regressed onto NOAA OLR that has been filtered using the KELVIN spectrum. In order to check the robustness of our wave composites for the IGRA radiosonde dataset, we perform these regressions twice with two independent rainfall proxy datasets: filtered TRMM 3B42 over the interval 1 January 1998 – 31 December 2011; and filtered NOAA OLR over the interval 1 January 1982 – 31 December 1997. We repeat this analysis with other IGRA stations around the tropical band, but do not analyze them in detail in this work.

To form WPAC group composites from ERAI, FNL, T255-OPANA, and T255-LAND, we use the nearest spatial grid points to each respective WPAC group station to represent members of each composite. For ERAI and FNL, we use the years 2000-2013 for both NOAA OLR and TRMM 3B42 rainfall proxies to take advantage of the period for which all these data overlap. For T255-OPANA, we use the years 2008-2013 and form composite regressions using NOAA OLR, TRMM 3B42, and also the ECMWF OLR. For T255-LAND and the ECMWF aqua-planet integrations, we only use the ECMWF OLR, since

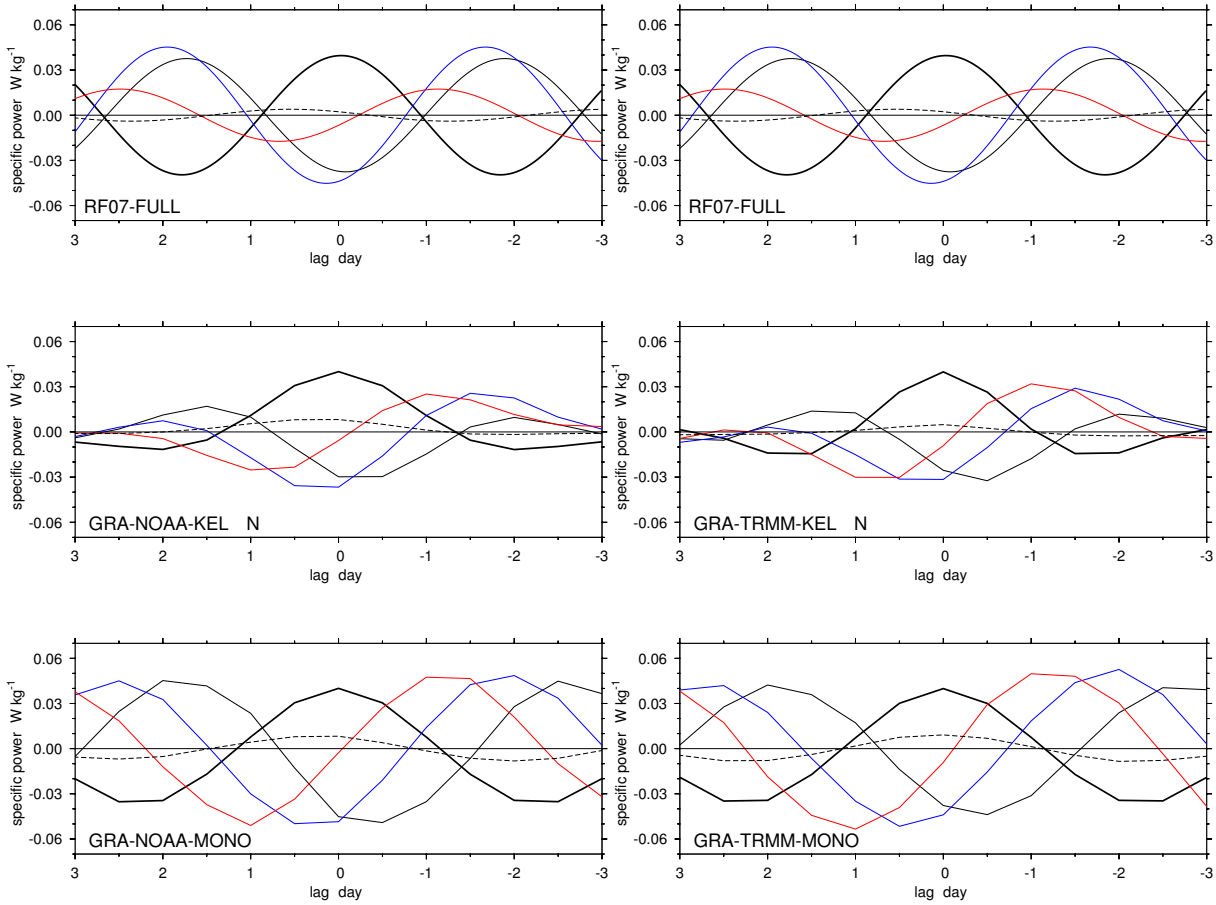

Figure 3: As in Figure 1, except for wave composites from radiosonde stations in the West Pacific (i. e., the WPAC group). Results for the KELVIN (middle) and MONO (bottom) filters are shown for NOAA OLR 1982-1997 (left), and for TRMM 3B42 1998-2013 (right). The full RF07 model plot is placed atop each column to facilitate comparison.

these models don't assimilate observations. The lack of continents in the aqua-planet models eliminates the focusing effect that gives wave species preferred spatial locations in the real atmosphere, which reduces the signal-to-noise ratio at any given location along the aqua-planet tropical band. We thus choose twenty-five regularly-spaced points along the zonal axis in the respective region of greatest CCKW variance for each model to represent discrete locations of interest. These locations are then averaged together into composites as in the models with orography.

4 Results

In this section we show how the phase relationships and the amplitudes of deep convective inhibition DCIN and column moisture as well as vertical structures of temperature and zonal wind from radiosonde data, analysis and reanalysis data and the various ECMWF runs compare to the RF07 linear model theory as well as to each other. Most figures in this section illustrate composites of linear regressions from a set of locations in the West Pacific (IGRA, ERAI, FNL, OPANA, LAND) or else from a set of equidistant locations along the equator (ECMWF aqua-planets). The exception is a scatter plot showing all the IGRA stations used in this study.

4.1 Radiosonde data, analysis, and reanalysis data

Figure 3 shows the contributions to the precipitation decomposition, i. e., indices from RF07, as a function of lag time for the eastward-moving convectively coupled Kelvin mode based on observations in the WPAC group. The Kelvin-filtered (middle, KELVIN) and monochromatic wave-filtered (bottom, MONO) results are shown for regressions onto NOAA OLR 1982-1997 (left), and onto TRMM 3B42 1998-2013 (right). The RF07 linear model result is placed atop each column to facilitate comparison. The total precipitation is given by a thick solid line, the column moisture contribution P_1 by a dashed line, the total DCIN contribution by a thin solid black line, the DCIN contribution due to changes in buoyancy of air above the boundary layer P_{2t} is shown in blue, and the DCIN contribution due to boundary layer moist entropy anomalies P_{2s} is shown in red. Note that the total precipitation predicted by the RF07 linear model, (6), is not shown, but has roughly the same amplitude and lies slightly to the right of the filtered rainfall shown in the plot.

The middle plots show results from the full Kelvin-band filter (KELVIN). Since this filter represents a broad spectrum of frequencies and wavenumbers, the resulting structures are linear combinations of these and thus resemble a wave packet. The bottom plots show results for the monochromatic filter (MONO), which has a narrow frequency band centered at a period of $T = 4.5$ d.

The Kelvin band filter shows small differences in period between rainfall proxies, since each projects onto spectral modes differently. This is primarily due to a considerable difference in spatial and temporal resolutions. The Kelvin wave represented by filtered NOAA OLR shows a period of $T \approx 4.2$ d, while that of the filtered TRMM 3B42 resolves shorter periods and wavelengths, giving a period of $T \approx 3.5$ d; the former is closer to the observed CCKW OLR variance spectral maximum of $T \approx 5.5$ d near $l \approx 5$ (Kiladis *et al.* 2009). Nevertheless, the periods and phase relationships between the plotted indices are very similar for the two rainfall proxies, as well as between the two filtering bands. In addition, the periods agree with those of the temperature and specific humidity anomalies at Majuro shown in Figure 8 of (Kiladis *et al.* 2009).

The amplitudes of these indices differ between the filtering bands (KELVIN vs. MONO) due to the tapering effect of the wave packet envelope, i. e., the linear superposition of a broad spectrum of wavenumbers and frequencies. This point highlights the importance of the monochromatic filter, which allows amplitudes to be more readily compared across the lag axis. We should note, however, that since the MONO filter selects a narrow subset of the spectrum, it is subject to greater variability between datasets (illustrated below). Although amplitudes are distorted in the KELVIN results, the filter is useful for its added statistical robustness as well as for comparing the weight of high versus low frequency rain events in the broader KELVIN filter. The general agreement among wave filters suggests they independently illustrate real and salient features of the CCKW.

We now compare the WPAC group results to the linear model of RF07 (top row in Figure 3). The resulting wave period $T = 3.7$ d and phase speed $c = 18$ m s^{-1} are consistent with the assumed wavenumber $l = 7$ in that model. The phase relationships among all the variables show strong similarity with the exception of the column moisture. In the linear model, the column moisture P_1 (dashed) lags the rainfall anomaly by nearly one day and is thus in quadrature with the rainfall, while in the WPAC group these are nearly in phase. The amplitude of P_1, however, is small in both the linear model and in the composites.

A more significant difference arises in the amplitudes of the DCIN indices. In RF07-FULL, the threshold entropy P_{2t} (blue) is the most significant index, with amplitude similar to the rainfall. This index drives changes in the DCIN largely by itself. In contrast, the boundary layer moist entropy P_{2s} (red) has half the amplitude of P_{2t}. The noted predominance of P_{2t} supported the conclusion in RF07 that rainfall during

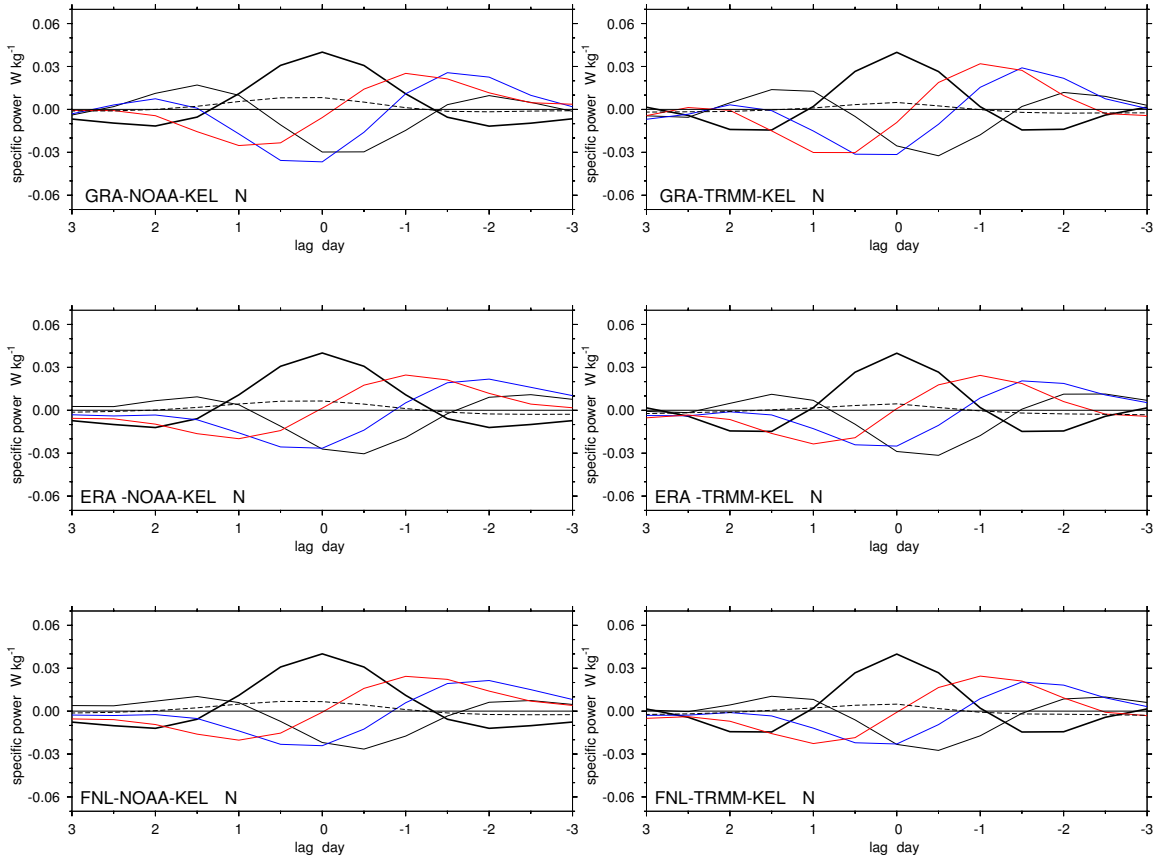

Figure 4: As in Figure 3, except for KELVIN composites of ERAI reanalysis (middle) and FNL analysis (bottom) for the WPAC group. Results are shown for NOAA OLR 1982-1997 (left), and for TRMM 3B42 1998-2013 (right). Corresponding IGRA radiosonde composites are placed atop for comparison.

CCKW events is almost entirely driven by the threshold temperature anomaly—a direct effect of the adiabatic motion of the CCKW.

Each corresponding index in the WPAC group has amplitude similar to that of RF07-FULL except for the boundary layer moist entropy P_{2s}. In the data, the amplitude of this index is approximately that of P_{2t}. This suggests the two atmospheric layers work together to form a convective inhibition anomaly. If the real moisture anomaly were less significant the minimum in DCIN would occur later, perhaps after the rainfall maximum at more positive lag. Since the DCIN minimum generally precedes or coincides with the rainfall anomaly in the WPAC group, it is a possible causal mechanism for the CCKW rainfall anomaly. This supports the conclusions of RF07.

Figure 4 shows the Kelvin-filter results from the ERAI reanalysis (middle) and the FNL analysis (bottom). These closely resemble the composites from IGRA radiosonde stations. The MONO results for these models (not shown) are also very similar to the corresponding radiosonde composites with matching amplitudes for all datasets and rainfall proxies. The match to ERAI and FNL is not surprising, considering that these models both assimilate data from the WPAC group IGRA stations; although each analysis also depends on a forecast model, which likewise plays an important role in matching the observations.

We also looked at a range of other radiosonde stations around the tropical band to check if the pattern

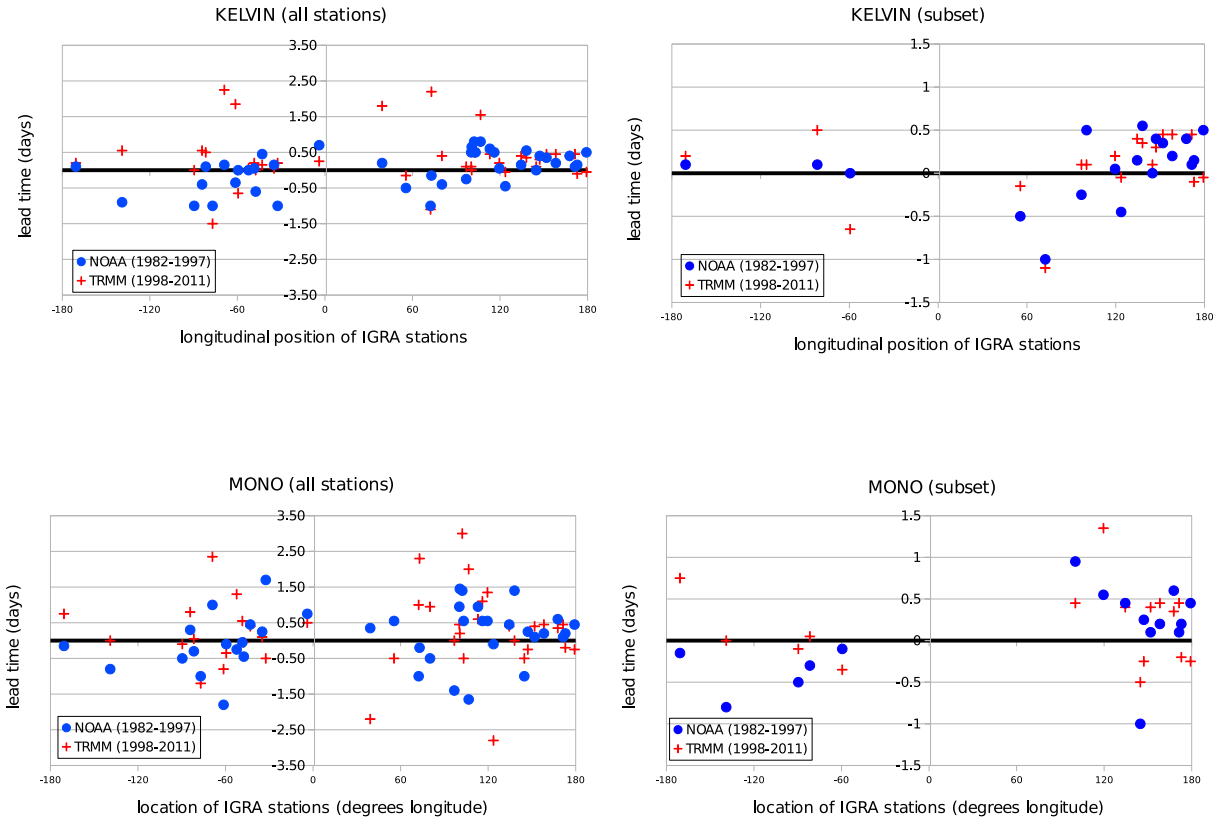

Figure 5: Scatter plots showing lead time of DCIN minimum over precipitation maximum versus IGRA station longitude for the KELVIN (top) and MONO (bottom) filters. Results for NOAA (blue circles) and TRMM (red crosses) are shown for all IGRA stations examined in this study (left) and for a subset including only island-based stations where the NOAA and TRMM results agree by better than 1 *d.*

of DCIN minimum preceding the rainfall maximum is robust. Figure 5 shows the number of days the DCIN minimum leads the rainfall maximum as a function of station longitude for KELVIN (top left) and MONO (bottom left) filters. Statistical differences between the rainfall proxies are evident in the plots: TRMM (red crosses) has more scatter—likely an effect of the finer resolution of this dataset, which could lead to greater sensitivity to local convective events not associated with CCKWs. The MONO filter has more scatter than the KELVIN filter, likely due to the smaller number of wave events entering the composite in that case. The scatter for both rainfall proxies is also partly due to the fact that our limited time resolution gives an uncertainty of ± 6 h. Lastly, there should be some systematic error associated with the rainfall-OLR relationship.

These caveats aside, a majority of the points are above the zero axis in both plots, indicating that for most of the stations, the DCIN minimum precedes or is in phase with the rainfall anomaly. To eliminate potentially erroneous outliers, the plots at right show only island stations where the estimated lead times derived from the independent datasets NOAA OLR and TRMM 3B42 differ by less than 1 d. Stations in Figure 2 with concentric circles survive this discrimination procedure. Again, results for KELVIN (top) and for MONO (bottom) are shown. The reason for this selection is to eliminate stations on large land masses that might distort the behavior of CCKWs over open ocean, and also to eliminate cases where the behavior at a single station during a particular observation interval is dominated by an unusual event. Recall that the two rainfall proxies are not merely independent in the sense that the data originates from different sensing instruments, but also in the sense that they cover distinct time intervals.

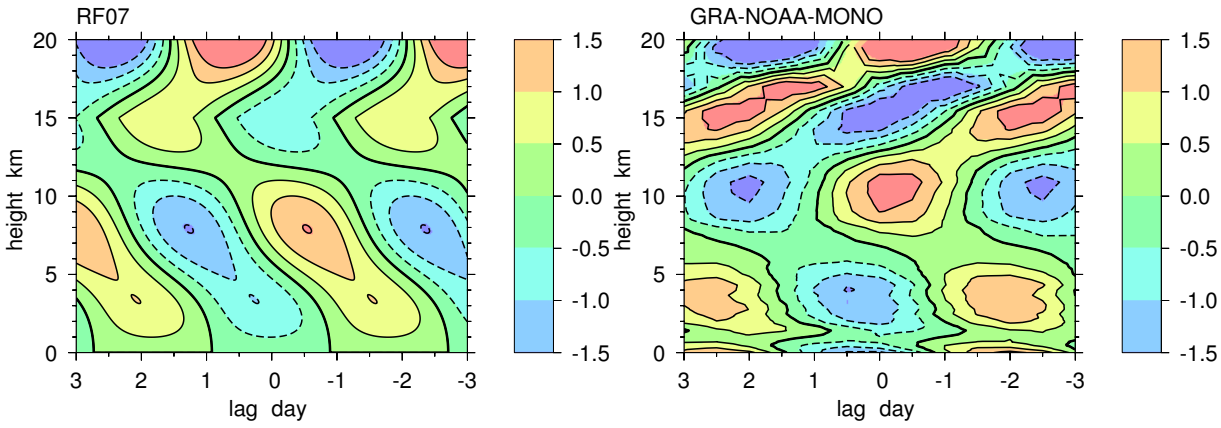

Figure 6: The temperature perturbation (K) vertical structure of the eastward-moving Kelvin mode for the RF07 linear theory (left) and from IGRA WPAC group using the MONO filter and NOAA OLR (right).

Without outliers, the bias towards positive lead times is more evident. In addition, the WPAC group (east of 120°) stations have robustly positive lead times, with an average near $\Delta t \approx 6$ h for the Kelvin-filter. Again, the MONO filter shows greater variability, but here the results also suggest a positive lead bias in the West Pacific. It is no coincidence that these stations survive this unbiased selection procedure: they are closest to the global precipitation variance maximum for CCKWs. The outlier that remains to the East of 120° longitude in the KELVIN scatter plot is Kupang Penfui (123.67,-10.17), at the southern edge of Indonesia. For the MONO plot, the most extreme outlier is Agana (144.8, 13.48). Both of these stations experience considerably weaker CCKW variance than all other stations in the region (see Figure 2).

The radiosonde stations that show the most robust DCIN-rainfall relationship are therefore those in the northern West Pacific. Since the CCKW signal is most prominent in that region (Wheeler and Kiladis 1999; Roundy and Frank 2004) the strong concensus on Kelvin-filtered wave phenomena there combined with the theory of RF07 suggests that DCIN control is a causal mechanism for the destabilization and propagation of these waves.

It is also notable that several stations that survive the discrimination procedure for the KELVIN filter lie to the West of the WPAC group and show robustly *lagging* DCIN. The greatest lag is near the center of the Indian Ocean at Diego Garcia (72.4,-7.3) and at Seychelles (55.53,-4.67). This is intriguing evidence of the existence of the extra variability in Indian Ocean CCKWs noted by (Roundy 2012a,b). To check if this variability is dependent on the timescale of the wave, we also examined the results of a modified MONO filter using the same wavenumber, but with oscillation period $T = 8$ d (not shown). We found that the modified filter gave similar phase relationships at Majuro, but not at Diego Garcia. While we only examined two stations using the modified filter, this result further supports the notion that a continuum of physical mechanisms exists for CCKWs that propagate at different speeds in the Indian Ocean.

It should be noted here that the lead in DCIN with respect to the rainfall anomaly suggested by these plots may actually be smaller than what is seen in the WPAC group. Since each of our rainfall proxies is comprised of satellite observations, we are not strictly analyzing the DCIN-rainfall relationship here. If an additional lag exists between rainfall and the proxies used here, though, it is likely less than the temporal resolution of our study. Haertel and Kiladis (2004) found that a satellite brightness temperature minimum lagged a budget-derived rainfall anomaly by approximately 4 h in composite two-day waves derived from the Tropical Ocean Global Atmosphere Coupled Ocean-Atmosphere Response Experiment (see their figure 2). In addition, Rickenbach *et al.* (2008) estimated the lag between rainfall maxima

and anvil area maxima for convective towers over Florida to be $1-2$ h, but also suggested this time could increase for larger systems. Nevertheless, the scatter plots shown in Figure 5 illustrate the fact that CCKWs have a typical DCIN phase signature, whereby the DCIN anomaly slightly precedes the rainfall anomaly.

Figure 6 shows the vertical structure of the temperature anomaly for the eastward-moving CCKW in the $x-z$ plane for the RF07 model (left) and for the WPAC group composite using NOAA OLR (right). We use the MONO filter to form composites in this figure to facilitate comparison to the RF07 linear model, and we scale all variables to the same rainfall anomaly at $t = 0$ d as in the phase plots. The vertical temperature structures are broadly similar, in both the characteristic boomerang structure with westward-tilting (towards greater lag times) contours in the low to middle troposphere and eastward tilt above. While the elbow is higher in the RF07 model than in observations, the overall tilted structure matches the findings from observations (Wheeler *et al.* 2000; Straub and Kiladis 2002) and from cloud resolving numerical simulations (Peters and Bretherton 2006; Tulich *et al.* 2007).

Differences include the sign of the anomaly in the upper troposphere and lower stratosphere, which completes the boomerang shape in the composites, and the lack of surface temperature anomalies in the linear model. The latter deficiency is due to the specified boundary-conditions, which could affect the strength of the boundary layer moist entropy anomaly. Furthermore in the model, the maximum temperature anomaly occurs at 8 km, near $t = -.75$ d while in the composites this occurs at 10 km, at $t = 0$ d. There is furthermore a temperature maximum near $z = 3.5$ km, $t = -2$ d that is less prominent in the model.

4.2 ECMWF operational analysis and annual integrations

We now consider the behavior of the RF07 indices in a set of long integrations with the ECMWF model. Figure 7 shows composited indices from the ECMWF operational analysis (T255-OPANA, 2nd row) and the freely-running one-year integrations with the same model (T255-LAND, 3rd row). The KELVIN composites are at left and the MONO composites are at right. For comparison, corresponding ERAI results are displayed at the top of the figure. The ERAI reference composites are derived from NOAA OLR, but the TRMM 3B42 results are similar.

These data have half the temporal resolution of ERAI, so features appear more irregular, though T255-OPANA indices seem to match those of ERAI quite well. This is what we expect, since much of the same physics and observational data enters both analyses. It is difficult to compare amplitudes due to the lower resolution of the operational analysis, but the phase relationships match ERAI for both the KELVIN and MONO composites. The DCIN index minimum precedes the rainfall maximum in both cases by ≈ 6 h. Recall that this is the lead time that appears for the West Pacific CCKW in the scatter plots of Figure 5.

In the freely-running integrations, however, significant changes occur in the RF07 indices. Firstly, the column moisture anomaly (dotted) falls well past the rainfall anomaly, peaking near $lag = +1$ d for both wave filters. The threshold entropy anomaly P_{2t} (blue), however, peaks near $lag = -2$ d in both filters, and the phase and amplitude of this index approximate the ERAI results.

The important difference here is that the boundary layer moist entropy anomaly P_{2s} (red) is significantly smaller in T255-LAND than in both ERAI and T255-OPANA. It also arrives earlier in the MONO case, but that appears not to be robust, as is shown below. The end result is the same in both cases, however, regardless of the phase of P_{2s}: the DCIN minimum occurs after the rainfall anomaly, near $lag \approx +1/3$ d. The free-run ECMWF (T255-LAND) simulation thus seems to lose something when not coupled to assimilated data. Uncharacteristic behavior in the RF07 indices occurs with a diminished CCKW

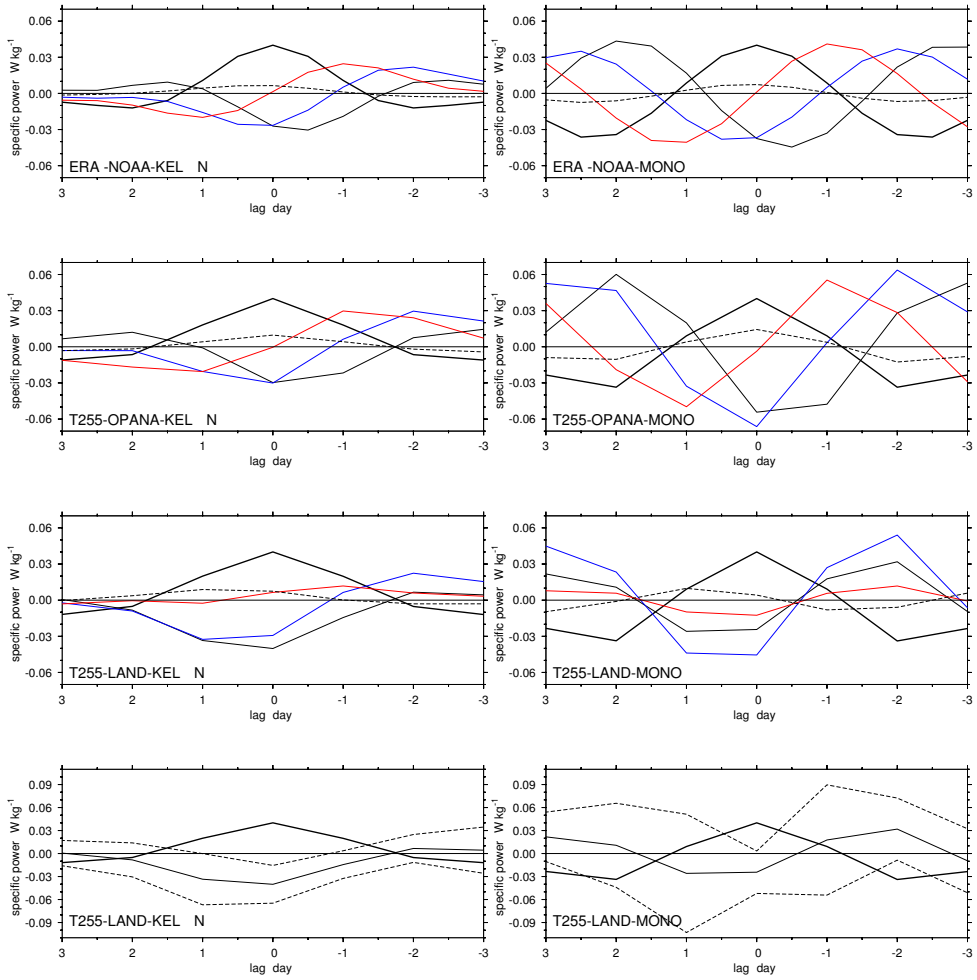

Figure 7: As in Figure 3, except for the KELVIN (left) and MONO (right) results for ECMWF operational analysis (2nd row) and ECMWF free-run simulation with orography (3rd row). 95% confidence intervals for the DCIN estimates in the ECMWF free-run simulation with orography are shown in the bottom row with a slightly broader vertical axis. The corresponding ERAI analyses with NOAA OLR (1982-1997) are placed atop each column for comparison.

variance in the T255-LAND model, compared to T255-OPANA. Figure 8 shows contours of standard deviation in KELVIN-filtered OLR during six years of model output for both T255-OPANA and T255-LAND. The corresponding observed standard deviation from TRMM 3B42 is plotted in 2 using the same contours. The standard deviation is less in the free-run than in the operational analysis. Since the DCIN-OLR relationship differs significantly between the freely-running integrations and the analysis, the reduced variance of CCKWs in the West Pacific of T255-LAND supports the notion that DCIN plays a causal role in the formation and propagation of CCKWs.

To check the statistical significance of these results, we examine the standard deviation of the mean DCIN index across the ensemble of WPAC group locations entering the composite, shown at bottom, Figure 7. For each wave filter, the DCIN and 95% confidence intervals ($\pm 2\sigma$) around the ensemble mean value are plotted with the respective rainfall anomalies. The variance is small for the Kelvin-filter, which makes sense given the averaging effect of the broad-spectrum filter, and the DCIN minimum appears to occur after the rainfall peak within $\pm 2\sigma$. The variance around the DCIN minimum for the MONO filter is

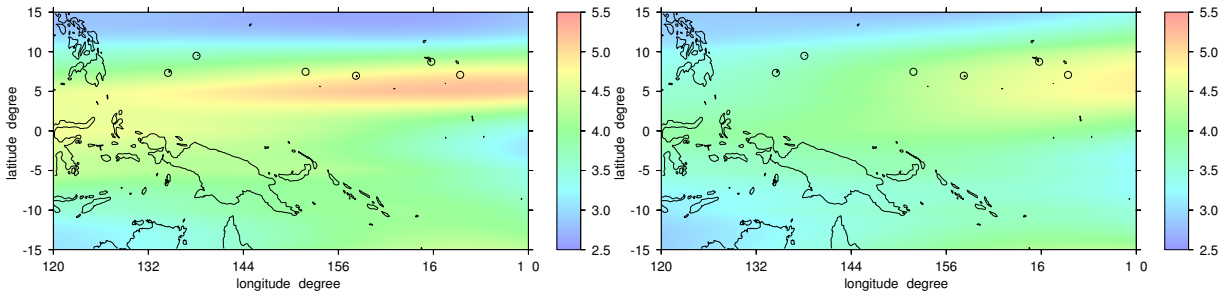

Figure 8: Contours of the square root of the variance (standard deviation) of KELVIN-filtered ECMWF OLR for T255-OPANA (left) and T255-LAND (right). The OLR has been scaled to the rainfall rate (mm d^{-1}). WPAC group stations are marked with circles.

greater and the result is less clear. Nevertheless, there is evidence that the CCKW DCIN signature is altered in the freely-running model compared to the analysis.

We now examine the behavior of the ECMWF model in the absence of land with a variety of spatial resolutions. We also run the model with the deep convective parameterization scheme turned off in order to discern its effect upon CCKW signatures.

Plots of RF07 indices versus lag time are shown in Figure 9. Reference plots from ERAI are placed atop each column for comparison and both KELVIN (left) and MONO (right) results are shown. The temporal resolution of the output data in the aqua-planet runs is reduced with respect to the ERAI. The most notable difference between the real Earth integrations with orography and the aqua-planet models is the reduction in all amplitudes—besides the rainfall—by a factor of two. This difference may be due to increased OLR variance in this model (see Appendix) and is an interesting difference between the ECMWF free-run with land (T255-LAND), and those without.

For the lowest resolution model ($\Delta x \approx 125$ km), the unusually broadened rainfall anomaly in the KELVIN filter plot shows that the greatest power in the CCKW spectrum lies at lower frequencies than in all other models of this study when the deep convective scheme is shutoff (T159-AQUA-NODEEP). The dominant wave period in this case is $T \approx 9$ d, which is twice the period defined by the MONO filter. Such broadening is not evident in the monochromatic case since the filter is too narrow to show this effect. In the low-resolution aqua-planet run without parameterized deep convection, the boundary layer moist entropy anomaly P_{2s} (red) is considerably larger than the threshold entropy anomaly P_{2t} (blue), which has the opposite effect as in T255-LAND. In this case, the large P_{2s} anomaly causes the DCIN minimum to precede the rainfall anomaly by 2 d.

It is interesting to see the effect of the deep convective scheme on this model. Looking at T159-AQUA-DEEP, we see the KELVIN wave packet is narrower than in T159-AQUA-NODEEP. Also, the P_{2s} anomaly is smaller, which drives the DCIN minimum toward the observed value.

This reduction of the P_{2s} anomaly is also evident between the two versions of the medium resolution ($\Delta x \approx 25$ km) model. Again, the P_{2s} anomaly is unusually large in T799-AQUA-NODEEP, so that the DCIN minimum appears near $lag \approx -1$ d. In T799-AQUA-DEEP, however, P_{2s} is smaller and the DCIN minimum is closer to the rainfall maximum, as in both ERAI and the radiosonde observations. Again, this reduction in P_{2s} occurs for both KELVIN and MONO when the deep convective scheme is turned on.

Lastly, we examine an aqua-planet employing the spatial resolution of the current forecast model ($\Delta x \approx$ 16 km), but without a deep convective scheme (T1279-AQUA-NODEEP). The P_{2s} anomaly is again

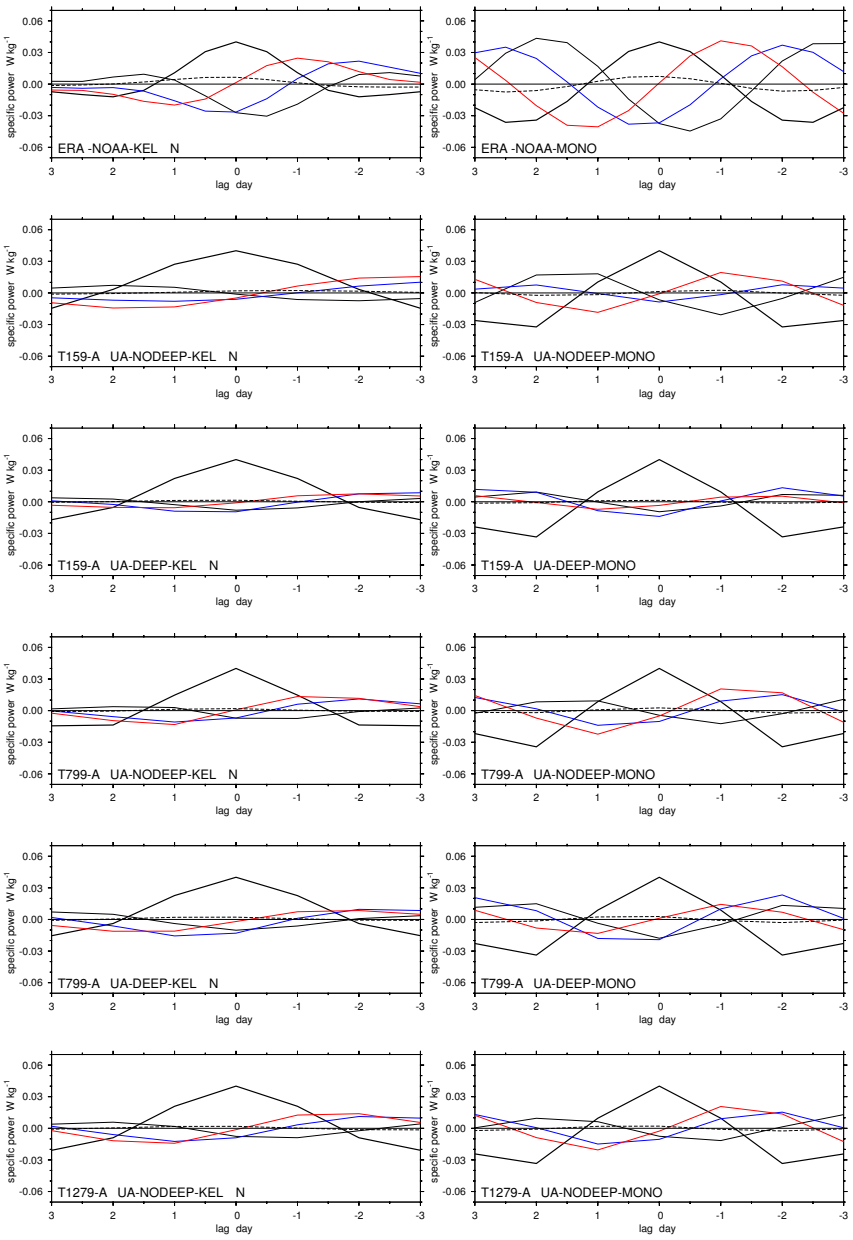

Figure 9: As in Figure 7, except for ECMWF aqua-planet models.

larger than in observations, which puts the DCIN minimum near $lag \approx -18$ h. In fact, the wave signature is very similar to that of T799-AQUA-NODEEP, suggesting that, even at this resolution, the grid-scale convection is not able to simulate a realistic CCKW without the deep convective scheme.

It is worth noting here that part of the difference in wave signatures could result from diminished or even missing spectral peaks within the filtering region. We checked this and found that the spectral peaks in each of the aqua-planet models are considerably more prominent than in the real atmosphere and in T255-LAND. This may explain the small thermodynamic anomalies in the aqua-planet models compared to the standard rainfall anomaly (50 mm d^{-1}) used. That is, if a given DCIN anomaly on the aqua-planet leads to much greater rainfall than in the real atmosphere, a more realistic rainfall event will correspond to a weaker DCIN anomaly in such a model.

The column moisture anomaly P_1 is small in all aqua-planet simulations. Also, it is in phase or slightly lags the rainfall maximum in every case, except for T159-AQUA-NODEEP. This odd behavior seems typical in such a course grid without the deep convective scheme.

We now examine the variance in the mean estimates for the aqua-planet indices. Figure 10 shows the DCIN anomaly estimate within 95% confidence intervals for each model shown in Figure 9 including ERAI. Only the aqua-planets lacking the deep convection scheme show greater uncertainty in the estimates of these curves than does ERAI. Again, there is considerably greater variance in the MONO estimates than in the KELVIN estimates. This supports the veracity of the broad-spectrum anomalies. However, note also that while the monochromatic DCIN estimates have large variance, it is uniform across the phase of the wave. This suggests that there are enough members included in each composite to accurately portray the characteristics of the wave.

Interestingly, the variance of the DCIN estimates decreases significantly when the deep convection scheme is included in the aqua-planet models T159-AQUA and T799-AQUA. This may be due to the fact that deep convective schemes help to quell instabilities in numerical models, which may prevent unusual thermodynamic fluctuations that would artificially increase the variance.

Figure 11 shows the vertical structure of the temperature anomalies for the ECMWF free-run with land (T255-LAND) and the highest resolution aqua-planet model (T1279-AQUA-NODEEP). All composites in this figure result from MONO filter regressions. The corresponding IGRA-NOAA and ERAI-NOAA plots are also shown for comparison. Both ECMWF runs show strong similarity to IGRA, with temperature anomalies centered near 4 km and near 10 km. While the amplitude of the aqua-planet model is diminished as in the aqua-planet phase plots, it nevertheless has maxima at these levels as well as the observed boomerang shape. In each case, there is a noticeable anomaly at the surface, and the phases of these anomalies are similar. Note that the ERAI anomalies are also diminished compared to IGRA results.

Figure 12 shows the vertical structure of the specific humidity perturbation for the same set of models. In this case, significant differences appear. While IGRA and T255-LAND have strong anomalies near and above the melting level, these anomalies are much weaker in ERAI. Indeed, there are problems with the humidity structure in ERAI due to biases in the moist physics of that model (Dee *et al.* 2011) and the fact that the vertical structure of humidity is less constrained than for temperature due to limitations in observational corrections to the short-range forecast. Were the forecast model of ERAI (the operational model in 2006) used for long integrations only weak CCKW would be produced (Bechtold *et al.* 2008; Hirons *et al.* 2012). However, the T255-LAND freely-running integrations, employing the more recent model cycle of 2013, also show a deficiency—namely an overly weak moisture anomaly in the lower troposphere with particularly weak anomalies near the top of the boundary-layer. In contrast, IGRA has nearly continuous anomalies over a deep layer extending upward from the boundary-layer. Importantly,

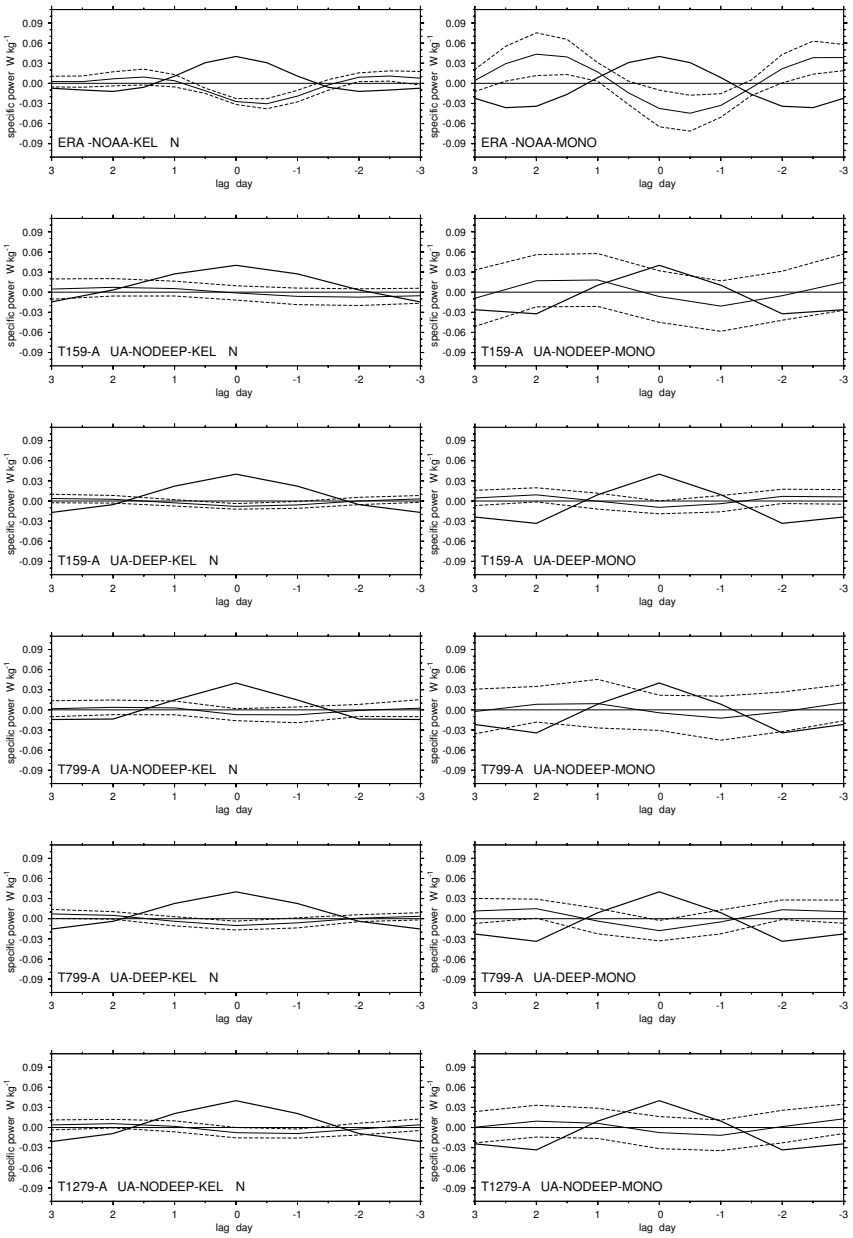

Figure 10: As in Figure 9, except for 95% confidence intervals for DCIN in ECMWF aqua-planet models. Note the vertical axes are slightly broader here to allow comparison with T255-LAND in Figure 7.

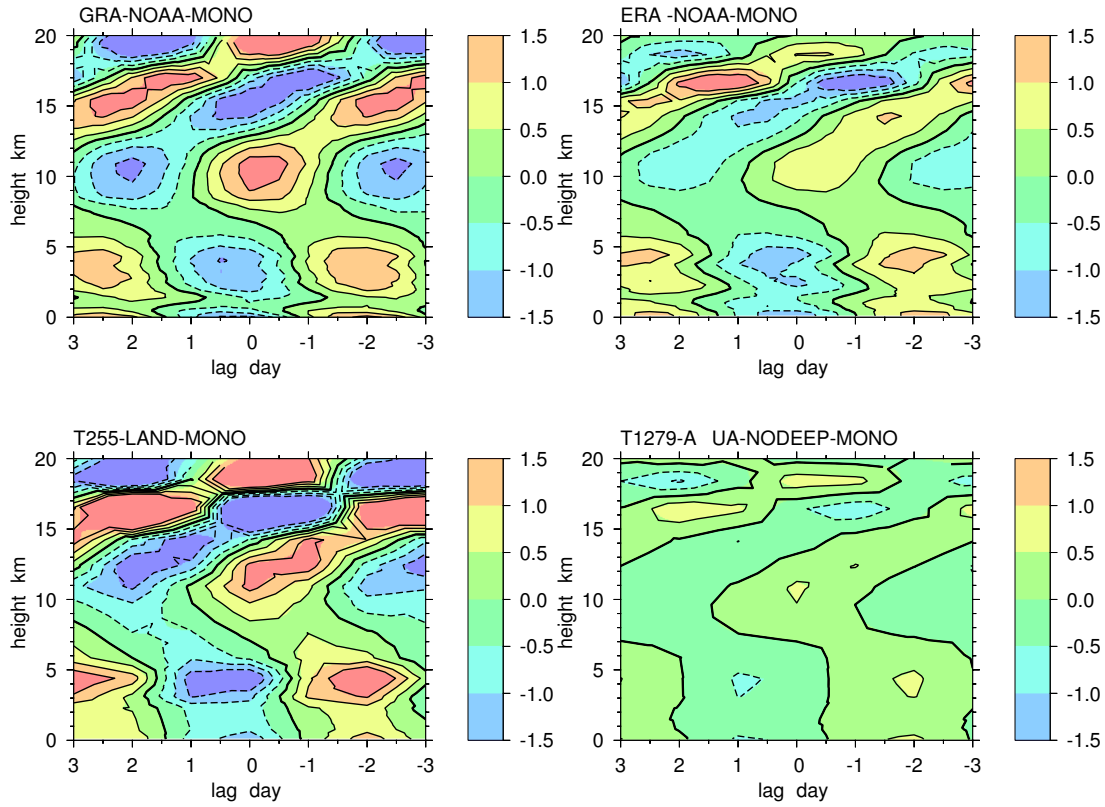

Figure 11: As in 6 but for the ECMWF free-run simulation with orography (bottom left), and the ECMWF highest-resolution aqua-planet model (bottom right). The IGRA-NOAA and ERAI-NOAA results are given on the top for comparison. All temperature anomalies are regressed onto the respective MONO rainfall proxy.

it is the moisture anomaly in the lower troposphere that is predominantly responsible for the unusual boundary layer moist entropy anomalies, P_{2s}, in figures 7 and 9.

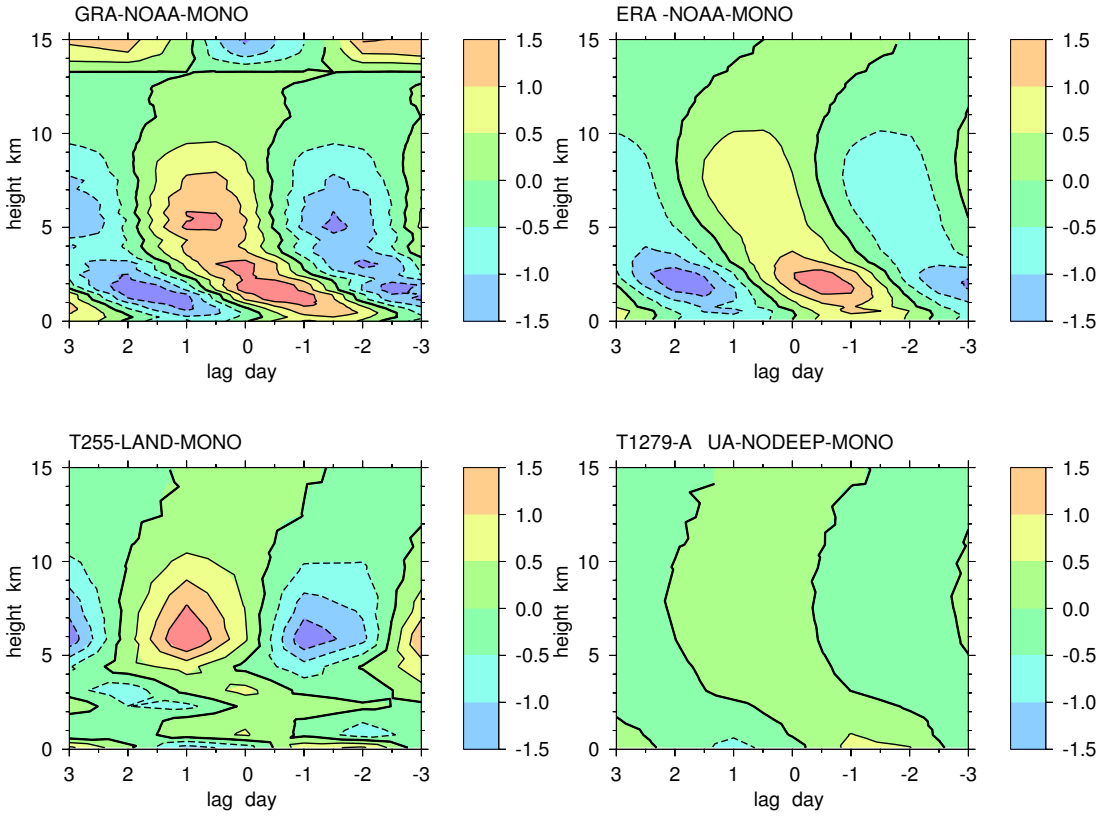

Figure 12: As in 11 except for specific humidity anomalies. Units are g kg^{-1}.

5 Conclusions

Composite structures of convectively-coupled Kelvin waves in the West Pacific and in other tropical locales were analyzed in terms of the linear theory of Raymond and Fuchs (2007, RF07) using radiosonde data, 3D analysis and reanalysis model output, and various ECMWF model simulations. We used five different thermodynamic data sources (IGRA, FNL, ERAI, ECMWF operational analysis, and freely-running one-year ECMWF integrations) and four different precipitation proxies (NOAA OLR, TRMM 3B42, ECMWF diagnosed OLR, and ECMWF diagnosed rainfall). The radiosonde composites were constructed using two independent datasets. Derived variables and indices representing deep convective inhibition and precipitable water from these datasets were used to examine the assumptions and conclusions of the RF07 theory.

We find that convective inhibition, represented here by the index DCIN, varies strongly with the CCKW precipitation anomaly. The DCIN anomaly appears to lead the rainfall on the average, but given uncertainties in the data, the amount of lead time is not clear. The unusual DCIN lag combined with reduced CCKW variance in the ECMWF freely-running real Earth simulation suggests the DCIN lead may be important. The DCIN-rainfall relationship is largely driven by fluctuations in the lower-tropospheric temperature, here represented by the saturated moist entropy. This temperature increases ahead of the rainfall and is closely followed by a boundary-layer moist entropy anomaly, shown here to be largely

a function of moisture fluctuations. Together, these variations comprise a significant minimum in convective inhibition that leads or is nearly in phase with the CCKW rainfall event. We found this to be true in every dataset and model we studied in regions where the CCKW variance is large. Since the RF07 linear model results in an unstable CCKW-like mode with realistic vertical structure even when the lower-tropospheric temperature anomaly alone modulates DCIN and thus the convective heating, we conclude that this temperature anomaly is at least as important as the moisture anomaly in driving these waves, and perhaps even causes the moisture anomaly. Since the RF07 model produces unstable Kelvin waves even when DCIN leads the rainfall by ≈ 1 h, a small lead in the real atmosphere is significant. The fact that DCIN leads the rainfall in both the RF07 model and in the real atmosphere, combined with the fact that the RF07 model produces unstable Kelvin waves when this is true suggests that DCIN plays a causal role in driving the deep convective phase of CCKWs.

While the above analysis describes CCKWs where the variance of filtered rainfall is large, there are interesting differences at other locales that deserve further study. In particular, stations in the Indian Ocean show a different rainfall-DCIN phase relationship that appears to be dependent on the disturbance period. This supports the findings of Roundy (2012a,b) and is further evidence that wave species in the Indian Ocean display a continuum of different phase speeds and physical mechanisms.

The boundary layer moist entropy varies more strongly in the real atmosphere than is predicted by RF07, but given the results of the linear model, it is unclear whether this variable is essential to the destabilization and propagation of CCKWs. The RF07 linear model has an unstable CCKW-like mode even in the absence of surface moisture flux feedback, suggesting the boundary layer moist entropy anomaly near $lag = -1$ d is not important. However, the contrast between ECMWF aqua-planet simulations with and without parameterized deep convection shows that this variable affects the physical realism of CCKWs. When the deep convective scheme is shutoff, convection is suppressed too long in this phase of the wave. Alternatively, Hirons *et al.* (2012) showed that if the deep convective scheme has weak entrainment, convection is triggered too early in this phase.

Precipitable water variations are considerably smaller than DCIN anomalies during the CCKW passage. We take this to mean that precipitable water has an insignificant effect on CCKWs and vice versa. This result is robust across all of our analyses and is in agreement with Roundy and Frank (2004) and also with Yasunaga and Mapes (2012a,b).

Caveats for this study include the fact that there is considerable random noise in the rainfall proxies and also in the thermodynamic data. This increases the scatter in the DCIN-rainfall relationship. Also, the noted time lag between the actual rainfall event and the OLR anomaly represents a small systematic error in the estimate of the phase relationship between DCIN and rainfall. In addition, the limited temporal resolution of the datasets used here creates uncertainty on the order of ± 6 h in the estimates of all phase relationships. In spite of these caveats, we find a consistent pattern among a broad variety of datasets: radiosondes, analysis, reanalysis, forecast model output, and even in the cloud resolving model results of Fuchs *et al.* (2014).

It is interesting to note that the tilted vertical structure in the RF07 model is a result of including DCIN in the convective closure. Evidence for this is seen in comparing Figure 5 of RF07, which includes DCIN, with Figure 4 of Fuchs and Raymond (2007), which doesn't include DCIN. The tilted structure is also robust to the choice of upper boundary condition, which we have verified by replacing the radiation upper boundary condition solution for one using a rigid lid (not shown). However, the tilted structure in this case neither corresponds to an unstable wave mode nor is unique. In the linear model of RF07, therefore, the radiation upper boundary condition is a necessary, but not sufficient, condition for the Westward tilt in an unstable wave mode. In contrast, Kuang (2008a) found a realistic tilted structure in numerical

simulations of convectively-coupled waves using a CRM linked with a linear wave model even when the linear model was capped by a rigid lid. In addition, Kuang (2008b) found unstable wave modes with realistic vertical structure in a toy linear model capped by a rigid lid. Thus, there is evidence that the lower arm of the characteristic boomerang structure—the westward tilt—in the temperature profile of CCKWs may be robust to the state of the upper boundary.

While the RF07 model assumes a single vertical heating mode, that of Kuang (2008b) uses two heating modes linked by the assumption that mid-tropospheric humidity modulates the depth of convection. While the latter mechanism may allow the linear model of Kuang (2008b) to exhibit realistic unstable waves beneath a rigid lid, the fact that the RF07 model yields realistic unstable waves when only a single heating mode—and a more realistic upper boundary—are assumed suggests the RF07 model contains sufficient physics for the destabilization of CCKWs. Since the RF07 model includes only very simple assumptions about the shape and phase of the heating, its realism supports the notion that the tilted structure is an effect of wave, not convective, dynamics.

CCKWs are generally fast-moving disturbances in which wave dynamics are important, while the integrated column water content—important in slow moving disturbances—does not play a major role. These waves appear to be controlled by changes in convective inhibition primarily due to changes in the buoyancy of air above the PBL. The low-level moisture anomaly that precedes these disturbances is also important as it affects DCIN. The phase relationships between precipitation maxima and anomalous DCIN, as well as the small amplitude precipitable water anomalies found in West Pacific IGRA radiosonde stations, the FNL analysis, the ERAI reanalysis, the ECMWF operational analysis, and in ECMWF aqua-planet simulations strongly supports our hypothesis that DCIN is the mechanism that destabilizes CCKWs and is the primary causal mechanism by which CCKWs control convection.

Acknowledgements

We thank Paul Roundy, Zhiming Kuang, and George Kiladis for their helpful reviews of our manuscript as well as for many discussions on the CCKW. We thank Patrick Haertel for discussions on convectively-coupled waves in general and for the perusal of TOGA-COARE CCW composites. We also thank Larry Oolman at the University of Wyoming for the use of many radiosonde data and George Kiladis and Maria Gehne at NOAA for providing an interpolated version of the IGRA radiosonde dataset. The TRMM 3B42 data used in this effort were acquired as part of the activities of NASA's Science Mission Directorate, and are archived and distributed by the Goddard Earth Sciences (GES) Data and Information Services Center (DISC) via the Mirador data portal. The SST climatology used in this study was obtained from the LDEO/IRI Data Library. Analysis (FNL) and reanalysis (ERAI) data were obtained from NCAR's Computational and Information Systems Laboratory (CISL) Research Data Archive. Derived data and coded routines used in this study are available from the corresponding author upon request.

This work was supported by U. S. National Science Foundation Grants ATM1021049 and ATM1342001, and also by the European Commission's 7th Framework Programme, under Grant Agreement number 282672, EMBRACE project.

Appendix

We now examine the differences between the ECMWF OLR and rainfall diagnostics. We found the correlation between these variables to be greatest at a lag of about 5 h, so that the rainfall diagnostic leads

the OLR diagnostic by this interval. A lagged relationship makes sense, since the cloud top temperature anomaly should evolve somewhat later than the mass flux that directly produces surface rainfall

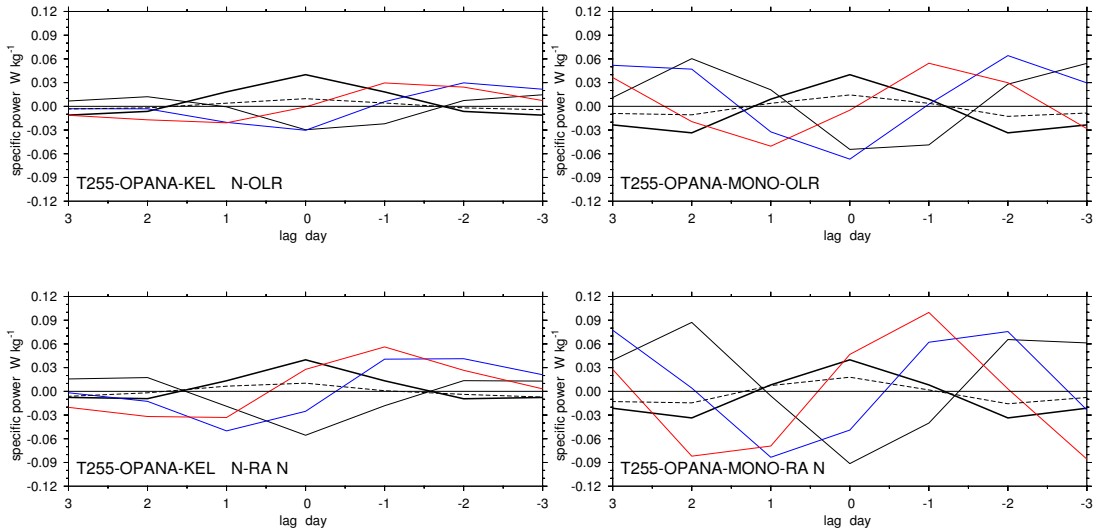

Figure 13: As in Figure 1, except for wave composites from T255-OPANA when using model OLR (top) and model rainfall (bottom) for both the KELVIN (left) and MONO (right) filters. Note the vertical axes are larger to accomodate the rainfall-regressed cases.

Figure 13 shows the RF07 indices for the ECMWF operational analysis, T255-OPANA, for both wave filters (KELVIN and MONO) and for both rainfall proxies available in the model (OLR and RAIN). These plots are shown with a larger vertical scale than the earlier plots to accommodate the surface rainfall results. The indices regressed onto the rainfall diagnostic have larger amplitude due to the smaller variance of the model rainfall compared to the other rainfall proxies used in this study.

The ECMWF rainfall standard deviation ($\sigma_{EC-RAIN} \approx 9$ mm d^{-1}) is roughly half that of the model's own OLR diagnostic (when scaled to units of mm d^{-1}; $\sigma_{EC-OLR} \approx 16$ mm d^{-1}), while both the NOAA OLR ($\sigma_{NOAA-OLR} \approx 18$ mm d^{-1}) and TRMM 3B42 ($\sigma_{NOAA-OLR} \approx 20$ mm d^{-1}) standard deviations are comparable to the model OLR. The resulting wave-filtered rainfall—also with small variance—then projects onto the more realistic assimilated thermodynamic anomalies. This in turn exaggerates the slope of the regression line, which amplifies the indices in the resulting composite. Apart from overall increased amplitudes, the most noticeable features are an increase in the amplitude of the boundary-layer moist entropy index (red) with respect to the threshold entropy (blue) and a lessening of the rainfall-DCIN lag. In the KELVIN case, the lag is negligible.

References

Andersen, J. A., and Z. Kuang, 2008: A toy model of the instability in the equatorially trapped convectively coupled waves on the equatorial beta plane. *J. Atmos. Sci.,* **65**, 3736–3757.

Back, L. E., and C. S. Bretherton, 2005: The relationship between wind speed and precipitation in the Pacific ITCZ. *J. Climate,* **18**, 4317–4328.

Bechtold, P., M. Köhler, T. Jung, F. Doblas-Reyes, M. Leutbecher, M. Rodwell, F. Vitart, and G. Balsamo, 2008: Advances in simulating atmospheric variability with the ECMWF model: From synoptic to decadal time–scales. *Quart. J. Roy. Meteor. Soc.,* **134**, 1337–1351.

Bretherton, C. S., T. Uttal, C. W. Fairall, S. E. Yuter, R. A. Weller, D. Baumgardner, K. Comstock, R. Wood, and G. B. Raga, 2004: The EPIC 2001 stratocumulus study. *Bull. Amer. Meteor. Soc.,* **85**, 967–977.

Dee, D. P., S. M. Uppala, A. J. Simmons, P. Berrisford, P. Poli, S. Kobayashi, U. Andrae, M. A. Balmaseda, G. Balsamo, P. Bauer, P. Bechtold, A. C. M. Beljaars, L. van de Berg, J. Bidlot, C. Delsol, R. Dragani, M. Fuentes, A. Geer, L. Haimberger, S. Healy, H. Hersbach, E. V. Hólm, L. Isaksen, P. Kalberg, M. Köhler, M. Matricardi, A. P. McNally, B. M. Monge-Sanz, J.-J. Morcrette, B.-K. Park, C. Peuby, P. de Rosnay, C. Tavolato, J.-N. Thépaut, and F. Vitart, 2011: The ERA–Interim reanalysis: Configuration and performance of the data assimilation system. *Quart. J. Roy. Meteor. Soc.,* **137**, 553–597.

Derbyshire, S. H., I. Beau, P. Bechtold, J.-Y. Grandpeix, J.-M. Piriou, J.-L. Redelsberger, and P. M. M. Soares, 2004: Sensitivity of moist convection to environmental humidity. *Quart. J. Roy. Meteor. Soc.,* **130**, 3055–3079.

Firestone, J. K., and B. A. Albrecht, 1986: The structure of the atmospheric boundary layer in the central equatorial Pacific during FGGE. *Mon. Wea. Rev.,* **114**, 2219–2231.

Fuchs, Ž., S. Gjorgjievska, and D. J. Raymond, 2012: Effects of varying the shape of the convective heating profile on convectively coupled gravity waves and moisture modes. *J. Atmos. Sci.,* **69**, 2505–2519.

Fuchs, Ž., and D. J. Raymond, 2007: A simple, vertically resolved model of tropical disturbances with a humidity closure. *Tellus A,* **59**, 344–354.

Fuchs, Ž., S. L. Sessions, and D. J. Raymond, 2014: Mechanisms controlling the onset of simulated convectively coupled Kelvin waves. *Tellus A,* **66**(0).

Grabowski, W. W., and M. W. Moncrieff, 2001: Large–scale organization of tropical convection in two–dimensional explicit numerical simulations. *Quart. J. Roy. Meteor. Soc.,* **127**, 445–468.

Haertel, P. T., and G. N. Kiladis, 2004: Dynamics of 2–day equatorial waves. *J. Atmos. Sci.,* **61**, 2707–2721.

Hirons, L., P. Inness, F. Vitart, and P. Bechtold, 2012: Understanding advances in the simulation of intraseasonal variability in the ECMWF model. Part II: The application of process based diagnostics. *Quart. J. Roy. Meteor. Soc.,* **139**, 1427–1444.

Khouider, B., and A. J. Majda, 2006a: Multicloud convective parametrizations with crude vertical structure. *Theor. Comput. Fluid Dyn.,* **20**, 351–375.

Khouider, B., and A. J. Majda, 2006b: A simple multicloud parameterization for convectively coupled tropical waves. Part I: Linear analysis. *J. Atmos. Sci.,* **63**, 1308–1323.

Khouider, B., and A. J. Majda, 2008: Equatorial convectively coupled waves in a simple multicloud model. *J. Atmos. Sci.,* **65**, 3376–3397.

Kiladis, G. N., M. C. Wheeler, P. T. Haertel, K. H. Straub, and P. E. Roundy, 2009: Convectively coupled equatorial waves. *Rev. Geophys.,* **47**(2).

Kuang, Z., 2008a: Modeling the interaction between cumulus convection and linear gravity waves using a limited–domain cloud system–resolving model. *J. Atmos. Sci.,* **65**, 576–591.

Kuang, Z., 2008b: A moisture–stratiform instability for convectively coupled waves. *J. Atmos. Sci.,* **65**, 834–854.

Kuang, Z., P. N. Blossey, and C. S. Bretherton, 2005: A new approach for 3d cloud resolving simulations of large scale atmospheric circulation. *Geophys. Res. Lett.,* **32**.

Lucas, C., E. J. Zipser, and B. S. Ferrier, 2000: Sensitivity of tropical west Pacific oceanic squall lines to tropospheric wind and moisture profiles. *J. Atmos. Sci.,* **57**, 2351–2373.

Majda, A. J., B. Khouider, G. N. Kiladis, K. H. Straub, and M. G. Shefter, 2004: A model for convectively coupled tropical waves: Nonlinearity, rotation, and comparison with observations. *J. Atmos. Sci.,* **61**, 2188–2205.

Majda, A. J., and M. G. Shefter, 2001a: Models for stratiform instability and convectively coupled waves. *J. Atmos. Sci.,* **58**, 1567–1584.

Majda, A. J., and M. G. Shefter, 2001b: Waves and instabilities for model tropical convective parameterizations. *J. Atmos. Sci.,* **58**, 896–914.

Maloney, E. D., and S. K. Esbensen, 2005: A modeling study of summertime east Pacific wind–induced ocean–atmosphere exchange in the intraseasonal oscillation. *J. Climate,* **18**, 568–584.

Mapes, B. E., 2000: Convective inhibition, subgrid–scale triggering energy, and stratiform instability in a toy tropical wave model. *J. Atmos. Sci.,* **57**, 1515–1535.

Matsuno, T., 1966: Quasi–geostrophic motions in the equatorial area. *J. Meteor. Soc. Japan,* **44**, 25–42.

Peters, M. E., and C. S. Bretherton, 2006: Structure of tropical variability from a vertical mode perspective. *Theor. Comput. Fluid Dyn.,* **20**, 501–524.

Raymond, D. J., 1995: Regulation of moist convection over the West Pacific warm pool. *J. Atmos. Sci.,* **52**, 3945–3959.

Raymond, D. J., and Ž. Fuchs, 2007: Convectively coupled gravity and moisture modes in a simple atmospheric model. *Tellus,* **59A**, 627–640.

Raymond, D. J., Ž. Fuchs, S. Gjorgjievska, and S. L. Sessions, 2015: Balanced dynamics and thermodynamic constraints in the tropical troposphere. *J. Adv. Model Earth Syst.,*. submitted.

Raymond, D. J., G. B. Raga, C. S. Bretherton, J. Molinari, C. López Carillo, and Ž. Fuchs, 2003: Convective forcing in the intertropical convergence zone of the eastern pacific. *J. Atmos. Sci.,* **60**, 2064–2082.

Raymond, D. J., and X. Zeng, 2005: Modeling tropical atmospheric convection in the context of the weak temperature gradient approximation. *Quart. J. Roy. Meteor. Soc.,* **131**, 1301–1320.

Rickenbach, T., P. Kucera, M. Gentry, L. Carey, A. Lare, R.-F. Lin, B. Demoz, and D. Starr, 2008: The relationship between anvil clouds and convective cells: A case study in South Florida during CRYSTAL–FACE. *Mon. Wea. Rev.,* **136**, 3917–3932.

Roundy, P. D., 2008: Analysis of convectively coupled Kelvin waves in the Indian Ocean MJO. *J. Atmos. Sci.,* **65**, 1342–1359.

Roundy, P. D., 2012a: Observed structure of convectively coupled waves as a function of equivalent depth: Kelvin waves and the Madden–Julian Oscillation. *J. Atmos. Sci.,* **69**, 2097–2106.

Roundy, P. D., 2012b: The spectrum of convectively coupled Kelvin waves and the Madden–Julian Oscillation in regions of low–level easterly and westerly background flow. *J. Atmos. Sci.,* **69**, 2107–2111.

Roundy, P. D., and W. M. Frank, 2004: A climatology of waves in the equatorial region. *J. Atmos. Sci.,* **61**, 2105–2132.

Sobel, A. H., S. E. Yuter, C. S. Bretherton, and G. N. Kiladis, 2004: Large–scale meteorology and deep convection during TRMM KWAJEX. *Mon. Wea. Rev.,* **132**, 422–444.

Straub, K. H., P. T. Haertel, and G. N. Kiladis, 2010: An analysis of convectively coupled Kelvin waves in 20 WCRP CMIP3 global coupled climate models. *J. Climate,* **23**, 3031–3056.

Straub, K. H., and G. N. Kiladis, 2002: Observations of a convectively coupled Kelvin wave in the Eastern Pacific ITCZ. *J. Atmos. Sci.,* **59**, 30–53.

Tulich, S. N., and B. E. Mapes, 2010: Multiscale convective wave disturbances in the tropics: Insights from a two–dimensional cloud–resolving model. *J. Atmos. Sci.,* **65**, 140–155.

Tulich, S. N., D. A. Randall, and B. E. Mapes, 2007: Vertical–mode and cloud decomposition of large–scale convectively coupled gravity waves in a two–dimensional cloud–resolving model. *J. Atmos. Sci.,* **64**, 1210–1229.

Wheeler, M., and G. N. Kiladis, 1999: Convectively coupled equatorial waves: Analysis of clouds and temperature in the wavenumber–frequency domain. *J. Atmos. Sci.,* **56**, 374–399.

Wheeler, M., G. N. Kiladis, and P. J. Webster, 2000: Large–scale dynamical fields associated with convectively coupled equatorial waves. *J. Atmos. Sci.,* **57**, 613–640.

Yasunaga, K., and B. E. Mapes, 2012a: Differences between more divergent and more rotational types of convectively coupled equatorial waves. Part I: Spacetime spectral analyses. *J. Atmos. Sci.,* **69**, 3–16.

Yasunaga, K., and B. E. Mapes, 2012b: Differences between more divergent and more rotational types of convectively coupled equatorial waves. Part II: Composite analysis based on space–time filtering. *J. Atmos. Sci.,* **69**, 17–34.

Yuter, S. E., and R. A. Houze, 2000: The 1997 pan american climate studies tropical eastern pacific process study. Part I: ITCZ region. *Bull. Amer. Meteor. Soc.,* **81**, 451–481.